NAVAL POSTGRADUATE SCHOOL
MONTEREY, CALIFORNIA

THESIS

BOTTOM BACKSCATTER MAPPING: THE
EFFECT OF SECONDARY MULTIPATH
INTERACTIONS

by

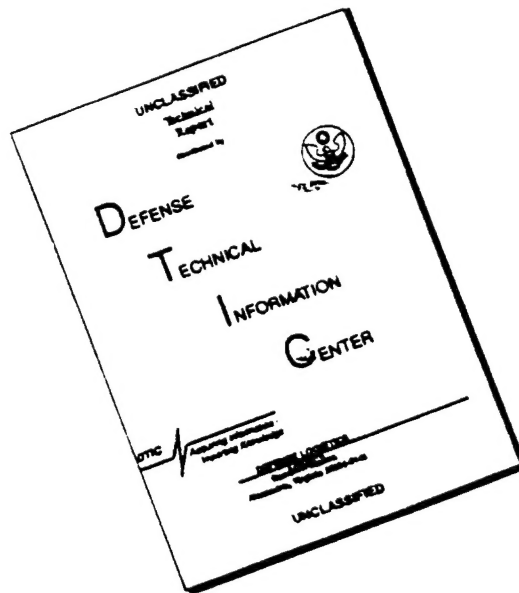Erick Brian Cushman

December, 1995

Thesis Advisor: Kevin B. Smith

Approved for public release; distribution is unlimited.

DISCLAIMER NOTICE

THIS DOCUMENT IS BEST QUALITY AVAILABLE. THE COPY FURNISHED TO DTIC CONTAINED A SIGNIFICANT NUMBER OF PAGES WHICH DO NOT REPRODUCE LEGIBLY.

REPORT DOCUMENTATION PAGE		Form Approved OMB No. 0704-0188

Public reporting burden for this collection of information is estimated to average 1 hour per response, including the time for reviewing instruction, searching existing data sources, gathering and maintaining the data needed, and completing and reviewing the collection of information. Send comments regarding this burden estimate or any other aspect of this collection of information, including suggestions for reducing this burden, to Washington Headquarters Services, Directorate for Information Operations and Reports, 1215 Jefferson Davis Highway, Suite 1204, Arlington, VA 22202-4302, and to the Office of Management and Budget, Paperwork Reduction Project (0704-0188) Washington DC 20503.

1. AGENCY USE ONLY *(Leave blank)*	2. REPORT DATE December 1995	3. REPORT TYPE AND DATES COVERED Master's Thesis	
4. TITLE AND SUBTITLE BOTTOM BACKSCATTER MAPPING: THE EFFECT OF SECONDARY MULTIPATH INTERACTIONS		5. FUNDING NUMBERS	
6. AUTHOR(S) Cushman, Erick B.			
7. PERFORMING ORGANIZATION NAME(S) AND ADDRESS(ES) Naval Postgraduate School Monterey CA 93943-5000		8. PERFORMING ORGANIZATION REPORT NUMBER	
9. SPONSORING/MONITORING AGENCY NAME(S) AND ADDRESS(ES)		10. SPONSORING/MONITORING AGENCY REPORT NUMBER	

11. SUPPLEMENTARY NOTES
 The views expressed in this thesis are those of the author and do not reflect the official policy or position of the Department of Defense or the U.S. Government.

12a. DISTRIBUTION/AVAILABILITY STATEMENT Approved for public release; distribution is unlimited.	12b. DISTRIBUTION CODE

13. ABSTRACT *(maximum 200 words)*

It has been shown that good correlation exists between large-scale, high level signal returns of bottom acoustic reverberation and bathymetric ridge structures. The ultimate goal of this type of analysis would be the removal of propagation effects resulting in a large-scale mapping of scattering strengths. Furthermore, analysis with a quasi-CW propagation model suggests a strong correlation between the small-scale fluctuations in the reverberation signal and the bottom acoustic ensonification, thereby suggesting that uncertainties in the predictions of forward propagation may limit the resolution of such mapping. By employing broadband modeling techniques, a valid representation of the complete time domain forward propagation is provided. Diffuse secondary bottom interactions appear to affect the resolution of the primary, direct-path interaction at ranges beyond a few water depths. Analysis of data recorded by near-bottom vertical line arrays (VLA's) confirms the existence of these secondary, multipath interactions in the forward propagation. The exact, two-way travel times from all bottom interactions are modeled and the influence of the secondary interactions is quantified. Possible ramifications for general sonar system performance are discussed.

14. SUBJECT TERMS Acoustic Propagation, Parabolic Equation Modeling, Secondary Multipath Interactions		15. NUMBER OF PAGES 62	
		16. PRICE CODE	
17. SECURITY CLASSIFICATION OF REPORT Unclassified	18. SECURITY CLASSIFICATION OF THIS PAGE Unclassified	19. SECURITY CLASSIFICATION OF ABSTRACT Unclassified	20. LIMITATION OF ABSTRACT UL

NSN 7540-01-280-5500

Standard Form 298 (Rev. 2-89)
Prescribed by ANSI Std. 239-18 298-102

BOTTOM BACKSCATTER MAPPING: THE EFFECT OF SECONDARY MULTIPATH INTERACTIONS

Erick B. Cushman
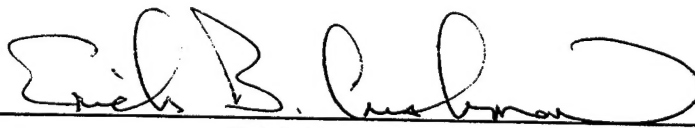Lieutenant, United States Navy
B.S.C.E., Tulane University, 1989

Submitted in partial fulfillment of the
requirements for the degrees of

MASTER OF SCIENCE IN PHYSICS
and
MASTER OF SCIENCE IN ENGINEERING ACOUSTICS

from the

NAVAL POSTGRADUATE SCHOOL
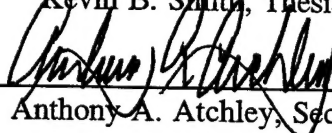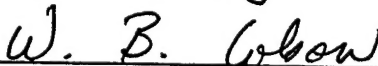**December, 1995**

Author: _____
Erick B. Cushman

Approved by: _____
Kevin B. Smith, Thesis Advisor

_____
Anthony A. Atchley, Second Reader

_____
William B. Colson, Chairman
Department of Physics

ABSTRACT

It has been shown that good correlation exists between large-scale, high level signal returns of bottom acoustic reverberation and bathymetric ridge structures. The ultimate goal of this type of analysis would be the removal of propagation effects resulting in a large-scale mapping of scattering strengths. Furthermore, analysis with a quasi-CW propagation model suggests a strong correlation between the small-scale fluctuations in the reverberation signal and the bottom acoustic ensonification, thereby suggesting that uncertainties in the predictions of forward propagation may limit the resolution of such mapping. By employing broadband modeling techniques, a valid representation of the complete time domain forward propagation is provided. Diffuse secondary bottom interactions appear to affect the resolution of the primary, direct-path interaction at ranges beyond a few water depths. Analysis of data recorded by near-bottom vertical line arrays (VLA's) confirms the existence of these secondary, multipath interactions in the forward propagation. The exact, two-way travel times from all bottom interactions are modeled and the influence of the secondary interactions is quantified. Possible ramifications for general sonar system performance are discussed.

TABLE OF CONTENTS

ACKNOWLEDGMENT

I. INTRODUCTION

In recent research conducted using data collected under the Acoustic Reverberation Special Research Project (ARSRP) sponsored by the Office of Naval Research, it has been shown that good correlation exists between large-scale, high level signal returns of bottom acoustic reverberation and bathymetric ridge structures. One may then attempt to obtain measures of bottom scattering strengths by removing the influence of propagation. Analysis with a quasi-CW propagation model, however, suggests a strong correlation between the small-scale fluctuations in the reverberation signal and the bottom acoustic ensonification. This suggests that uncertainties in the predictions of forward propagation may limit the resolution of such an inversion. The limits of the resolution of such a map are also imposed, in part, by the processing and the knowledge of the environment.

By employing broadband modeling techniques, a valid representation of the complete time domain forward propagation can be obtained. Despite the use of a directional vertical source array, diffuse secondary bottom interactions may affect the resolution of the primary, direct-path interaction at ranges beyond a few water depths. Analysis of data recorded by near-bottom vertical line arrays (VLA's) confirms the existence of these secondary, multipath interactions in the forward propagation. By computing the complex field at the bottom interface from both a vertical line array of sources and a point receiver, co-located in a monostatic geometry, the exact, two-way travel times and transmission loss from all bottom interactions can be determined. In this

1

manner, the influence of the secondary interactions on the measured bottom reverberation can be estimated.

The purpose of this thesis is to examine these effects and attempt to quantify them. Other issues are what level of resolution exists within the measured reverberation at ranges around one-half of the convergence zone distance and greater, and what level of resolution can model predictions hope to provide. Schemes for removing the influence of these secondary multipath interactions, if necessary, will also be discussed. Addressing these issues will advance the general knowledge of underwater acoustic propagation. Quantification of these influences and suggesting schemes to overcome them will lead to future improvements in sonar system design. The ability to resolve complex multipaths at significant ranges in a covert manner would provide great advantages to units involved in surveillance/power projection operations.

In Chapter II, some background information on the ARSRP experiment is provided. The numerical model used to predict acoustic propagation is also described along with other processing techniques used in the data analysis. In Chapter III, the existence of the secondary, multiple arrivals is confirmed in the measured data and compared with the forward propagation model predictions. The exact, two-way travel times and transmission loss are then modeled and the influence of the secondary interactions is quantified. Findings are summarized in Chapter IV and possible ramifications for general sonar system performance are discussed.

II. BACKGROUND INFORMATION

A.   THE ARSRP STUDY

In 1990, the Office of Naval Research (ONR) began an Acoustic Reverberation Special Research Program (ARSRP) in the area of underwater acoustic reverberation. The scientific plan for the bottom reverberation component of the ARSRP placed special emphasis on obtaining a detailed description of the bottom in the "natural laboratory" where acoustic experiments were to be conducted [Ref. 1]. The location of the ARSRP natural laboratory was selected to be on the west flank of the Mid-Atlantic Ridge (approximately 25° to 27° N and 45° to 50° W). Adequate environmental measurements could be obtained here in order to understand the connection between sea floor characteristics and scattering characteristics. Two geology and geophysics surveys were conducted of the region which resulted in data gridded at 200m × 200m. More detailed analysis was conducted at locations of particular interest providing information on the small-scale roughness spectra and bottom composition.

The ARSRP has conducted two acoustic field experiments in the region. An acoustic reconnaissance experiment was carried out in July-August 1991 aboard the Research Vessel (R/V) Cory Chouest [Ref. 2]. The major bottom reverberation experiment of the ARSRP was carried out in July 1993 [Ref. 3]. Three ships participated in the experiment - the R/V Cory Chouest, the R/V Alliance, and the R/V Knorr. The Cory deployed a vertical line source array and a horizontal line receive array, the

Alliance deployed a flextensional source (vertical pair) and a horizontal line receive array, and the Knorr deployed both near-bottom vertical line receive arrays and recording packages as well as the DTAGS (Deeply Towed Acoustics Geophysics System). Fig. 1 shows the ship tracks for the Cory and Alliance. A major emphasis of the experiment was on the collection of bistatic scatter from Sites A, B', and C'. Both the ship tracks and the transmission sequences for the Cory and Alliance were designed so that each ship would collect monostatic scatter from their own pings along with bistatic scatter from each other.

During the 1993 acoustics experiment, both the Cory and the Alliance made water column temperature and conductivity measurements. The Cory deployed 63 expendable bathythermographs (XBTs) as well as four expendable CTDs (1000m). The Alliance deployed 39 XBTs and made conventional CTD casts to full ocean depth at five locations.

B.   THE BEAMFORMER

The beamformer developed to process the transmission loss data output from the acoustic propagation model was written as a Matlab m-file. The m-file has been written to process the data from a 63-element vertical line array, which simulates the near-bottom vertical arrays used in the ARSRP study. Inter-element spacing of the simulated array is 1.95 meters. The actual arrays used in the study consisted of 59 elements, with an inter-element spacing of 2.07 meters. The important consideration for comparison of simulated and actual data is that their positions and total lengths are in agreement. The
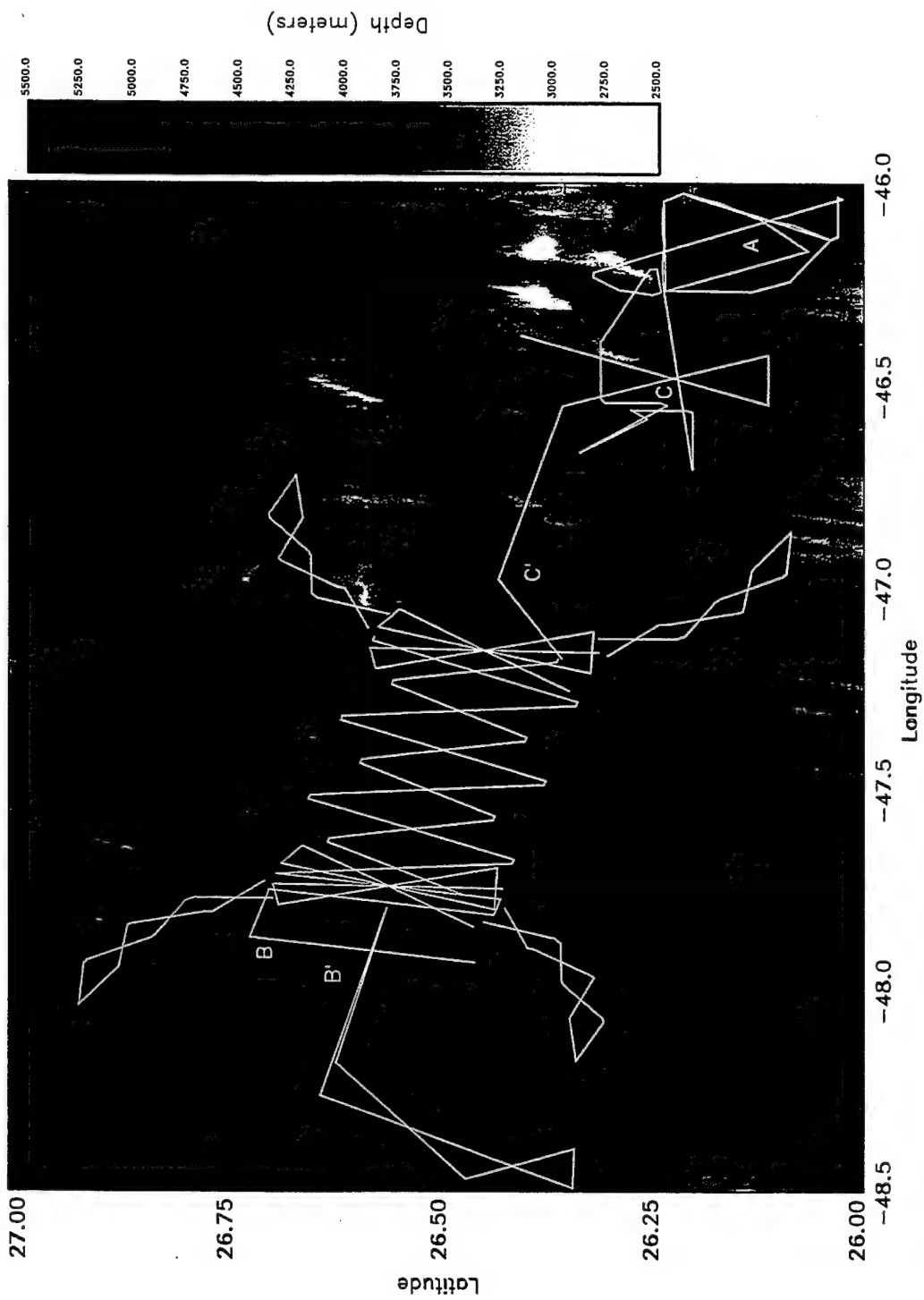
4

Figure 1. Ship tracks of R/V's Cory Chouest and Alliance during 1993 main acoustics experiment. From Ref. [4].

5

data is processed to produce a vertical arrival-angle versus time magnitude plot of the received sonar signal at the vertical array.

The beamformer is written for the specific output of the propagation model's broadband simulations. This data corresponds to a frequency bandwidth of 66.66 Hz with a center frequency of 227.5 Hz and a total of 1024 frequencies. Thus, incremental frequency spacing is 66.66/1024 = 0.065104 Hz. This results in a total Fourier-transformed time window of 15.36 seconds and a time resolution of 0.015 seconds.

These 1024 frequencies are placed in the positive portion of a frequency window which extends from -533.33 Hz to +533.33 Hz, with all other frequencies zero padded. A Blackman window is applied to the non-zero frequency information, and then the entire frequency window is transformed to the time domain resulting in a time window of 15.36 seconds long, but a time resolution of 9.4×10^{-4} seconds.

This time window is broken into thirty-one overlapping windows to take advantage of the increased time resolution and minimize sidelobe effects in time. Each overlapping window consists of 1024 sampled times, which are transformed back to the frequency domain where the frequency resolution is now 1.043 Hz. A Blackman window is now applied to the 63-element spatial array and transformed to the vertical wavenumber domain. Arrival angle information corresponds to wavenumber information as follows [Ref. 5]:

$$m = \frac{(N+Z)d\cos\psi_m}{\lambda} = \frac{(N+Z)d\cos\psi_m f}{c_o} \qquad (1)$$

6

where m is the wavenumber bin, N is the number of array elements, Z is the number of zeros that the FFT is padded with, d is the inter-element spacing, ψ_m is the arrival angle relative to endfire, λ is the wavelength, f is the frequency, and c_o is the reference sound speed of the water.

Once the arrival angle information is determined, the frequency window is finally transformed back to the time domain. The time domain information in the overlapping portions of the time windows are incoherently summed and the final matrix of arrival angle versus time is converted to transmission loss in dB (unnormalized) for plotting.

C.   THE ACOUSTIC PROPAGATION MODEL

The full-wave propagation method used to model the acoustic propagation for these studies uses a parabolic equation. Since the introduction of the parabolic equation method into the field of underwater acoustics in the 1970's by Hardin and Tappert [Ref. 6], the PE method has become a popular wave-theory technique for solving range-dependent propagation problems in ocean acoustics.

1.   Standard PE Derivation

The starting point in the derivation of the standard parabolic equation is the free-field Helmholtz equation for a constant-density medium in cylindrical coordinates (r, ϕ, z)

and for a harmonic field of time dependence exp($-i\omega t$),

$$\frac{\partial^2 p}{\partial r^2} + \frac{1}{r}\frac{\partial p}{\partial r} + \frac{\partial^2 p}{\partial z^2} + k_0^2 n^2 p = 0, \tag{2}$$

where azimuthal symmetry is assumed, $p(r,z)$ is the acoustic pressure, $k_0 = \omega/c_0$ is a reference wavenumber, $n(r,z) = c_0/c(r,z)$ is the index of refraction, and $c(r,z)$ is the sound speed describing the environment.

Assume the solution to Eq.(2) takes the form

$$p(r,z) = \psi(r,z) H_0^{(1)}(k_0 r), \tag{3}$$

which is an outgoing cylindrical wave solution. The envelope function $\psi(r,z)$ is assumed to be slowly varying in range. The Hankel function, which satisfies the Bessel differential equation

$$\frac{\partial^2 H_0^{(1)}(k_0 r)}{\partial r^2} + \frac{1}{r}\frac{\partial H_0^{(1)}(k_0 r)}{\partial r} + k_0^2 H_0^{(1)}(k_0 r) = 0, \tag{4}$$

can be replaced by its asymptotic form for $k_0 r \gg 1$,

$$H_0^{(1)}(k_0 r) \approx \sqrt{\frac{2}{\pi k_0 r}}\, e^{i(k_0 r - \pi/4)}. \tag{5}$$

Substituting Eq.(3) into Eq.(2), and using the Hankel-function property of Eq.(4), gives

$$\frac{\partial^2 \psi}{\partial r^2} + \left(\frac{2}{H_0^{(1)}(k_0 r)} \frac{\partial H_0^{(1)}(k_0 r)}{\partial r} + \frac{1}{r} \right) \frac{\partial \psi}{\partial r} + \frac{\partial^2 \psi}{\partial z^2} + k_0^2 (n^2 - 1)\psi = 0. \quad (6)$$

Making the far-field assumption, $k_0 r \gg 1$, Eq.(5) can be used to obtain the simplified elliptic wave equation

$$\frac{\partial^2 \psi}{\partial r^2} + 2ik_0 \frac{\partial \psi}{\partial r} + \frac{\partial^2 \psi}{\partial z^2} + k_0^2 (n^2 - 1)\psi = 0. \quad (7)$$

Next, the paraxial approximation is used to arrive at the standard parabolic wave equation. This small-angle approximation is expressed by

$$\frac{\partial^2 \psi}{\partial r^2} \ll 2ik_0 \frac{\partial \psi}{\partial r}. \quad (8)$$

A qualitative justification for this approximation can be made by noting that the main radial dependence of the field is contained in the Hankel function through the term $\exp(ik_0 r)$, while the envelope ψ will vary slowly with range over a wavelength λ. This can be expressed mathematically as $\partial \psi / \partial r \ll \psi / \lambda \sim ik_0 \psi$, or $\partial^2 \psi / \partial r^2 \ll ik_0 \partial \psi / \partial r$, and consequently the paraxial approximation is justified.

9

Making use of Eq.(8) in Eq.(7) results in

$$2ik_0 \frac{\partial \psi}{\partial r} + \frac{\partial^2 \psi}{\partial z^2} + k_0^2 (n^2 - 1)\psi = 0 ,$$

or   (9)

$$\frac{\partial \psi}{\partial r} = \frac{i}{2k_0} \frac{\partial^2 \psi}{\partial z^2} + \frac{ik_0}{2} (n^2 - 1)\psi ,$$

which is the standard parabolic equation.

2.   The Split-Step Fourier Algorithm

A second-order differential equation in r has now been reduced to a first-order one in r, allowing solutions by way of a non-iterative marching algorithm. Eq.(9) may be re-written as

$$\frac{i}{k_0} \frac{\partial \psi}{\partial r} = H_{op}\psi = (T_{op} + U_{op})\psi \tag{10}$$

where the operators

$$T_{op} = -\frac{1}{2}\left(-\frac{i}{k_0} \frac{\partial}{\partial z} \right)^2 = -\frac{1}{2k_0^2} \frac{\partial^2}{\partial z^2} , \tag{11}$$

10

and

$$U_{op} = U(r,\phi,z) = -\frac{1}{2}(n^2 - 1) . \tag{12}$$

This representation of the operators as kinetic and potential energy operators is especially insightful when it is desired to form the ray equations which have Hamiltonian form [Ref. 7]. In Eq.(10), the function ψ is a vector (in z) in Hilbert space. The values of ψ can now be expressed as

$$\psi(r + \Delta r) = \Phi(r)\,\psi(r) . \tag{13}$$

For all propagation predictions presented, we have employed the University of Miami Parabolic Equation (UMPE) model of Smith and Tappert [Ref. 8]. The UMPE model uses the split-step Fourier (SSF) method [Ref. 6] to compute the PE solution. This is accomplished by approximating the propagator function $\Phi(r)$ by

$$\Phi(r) \approx e^{-ik_0 \bar{H}_{op}(r)\Delta r} \tag{14}$$

where

$$\bar{H}_{op}(r) = \frac{1}{\Delta r} \int_r^{r+\Delta r} dr'\,H_{op}(r') . \tag{15}$$

This can be approximated by

$$\bar{H}_{op} = H_{op}(r + \frac{1}{2}\Delta r) , \tag{16}$$

11

or simply

$$\bar{H}_{op} = H_{op}(\mathbf{r}),\qquad(17)$$

which are referred to as "centered" and "endpoint" schemes, respectively. Presumably if the range step $\Delta \mathbf{r}$ is small enough the differences between the solutions are negligible. The UMPE model uses the approximation of Eq.(17).

The operator U_{op} is a multiplication operator in z-space and is therefore a diagonal matrix. The operator T_{op} is not diagonal in z-space, but is diagonal in wavenumber space. By separation of H_{op} into the two components T_{op} and U_{op} the propagator function becomes

$$\Phi(\mathbf{r}) = e^{-ik_0 \Delta \mathbf{r} T_{op}} e^{-ik_0 \Delta \mathbf{r} U_{op}},\qquad(18)$$

where the Baker-Campbell-Hausdorff expansion [Ref. 9]

$$e^{A+B} = e^A e^B e^{[A,B]+[A,[A,B]]+[B,[B,A]]+\dots}\qquad(19)$$

has been used. Since both T_{op} and U_{op} are small, their products are of second order and assumed negligible.

The general algorithm behind the PE/SSF implementation is then as follows. The PE field function ψ is specified at some range r in the z-domain. A transformation is made to the k-domain followed by a multiplication of the k-space operator $e^{-ik_0 \Delta \mathbf{r} \hat{T}_{op}}$. The result is then transformed again to the z-domain and is followed by a multiplication

12

of the z-space operator $e^{-ik_0 \Delta r U_{op}}$. The final result is the field function at $r + \Delta r$. The FFT subroutine employed in the numerical code assumes the convention

$$\psi(z) = \text{FFT}(\psi(k)) = \int \psi_{k_z} e^{ik_z z} \, dk_z \tag{20}$$

and

$$\psi(k) = \left[\text{FFT}(\psi^*(z)) \right]^* = \int \psi_z e^{-ik_z z} \, dz . \tag{21}$$

Therefore, the PE/SSF implementation can be represented by

$$\psi(r + \Delta r) = e^{-ik_0 \Delta r U_{op}(r,z)} \times \text{FFT}\left[e^{-ik_0 \Delta r \hat{T}_{op}(r,k)} \times \left[\text{FFT}(\psi^*(r,z)) \right]^* \right], \tag{22}$$

where, in k-space, the operator in Eq. (11) is given by

$$\hat{T}_{op}(k) = \frac{1}{2} \left(\frac{k_z}{k_0} \right)^2 , \tag{23}$$

and U_{op} is as defined in Eq. (12).

The UMPE model allows the user to choose from five different sets of operator forms. For the modeling used in this thesis, the higher order wide-angle approximation (WAPE) form [Ref. 9] has been used which is accurate to greater than $\pm$ 20° from the horizontal. The operator forms for the wide-angle approximation are

$$T_{\text{WAPE}} = \frac{\partial^2}{\partial z^2} \left[(1 + \frac{\partial^2}{\partial z^2})^{1/2} + 1 \right]^{-1} \tag{24}$$

13

and

$$U_{\mathrm{WAPE}} = -(n-1) \ .$$

(25)

In wavenumber space Eq.(24) may be written as

$$\hat{T}_{\mathrm{WAPE}}(k) = \left(\frac{k}{k_0}\right)^2 \left[\left(1 - \left(\frac{k}{k_0}\right)^2\right)^{1/2} + 1\right]^{-1} = 1 - \left[1 - \left(\frac{k}{k_0}\right)^2\right]^{1/2} \ .$$

(26)

Note that modes with $k > k_0$ are evanescent since

$$\hat{T}_{\mathrm{WAPE}}(k > k_0) = 1 - i\left[\left(\frac{k}{k_0}\right)^2 - 1\right]^{1/2} \ .$$

(27)

In the modeling done for this thesis, measured sound speed profiles from the Alliance CTD casts are used as input. The bottom is typically modeled as a single interface at depths extracted from the gridded database. The acoustic bottom properties are chosen to be representative of this area and have no lateral variability due to lack of geophysical data. Various analytical formulations of source functions are available; the point source and vertical line array were used in this work. Broadband UMPE model runs were performed to allow for more accurate investigations of the time domain response of the medium.

3. Computing One-Way (Forward) Travel Times

The UMPE code calculates the time domain arrival structure at a given range in a straight forward manner. The time harmonic acoustic field assumed by the model is given by

$$P(r,z,\omega t) = p_\omega(r,z)\, e^{-i\omega t}. \tag{28}$$

The representation in the time domain is then simply

$$\tilde{P}(r,z,t) = \text{FFT}\big[p_\omega(r,z)\big] = \int p_\omega(r,z)\, e^{-i\omega t}\, d\omega, \tag{29}$$

which follows from the realization that Eq.(28) is a single frequency component of the full-spectrum time dependent field given by Eq.(29).

To compute the arrival structure at some fixed range r=R, the model computes and stores the complex field values $p_{\omega,R}(z)$ for many frequencies and then Fourier synthesizes them to obtain $\tilde{P}_R(z,t)$, the set of complex pressure values in time/depth space. Because the FFT assumes inputs over the frequency band f_0 - BW/2 to f_0 + BW/2, where BW is the bandwidth of the acoustic source and f_0 is the center frequency, high frequency calculations can become computationally burdensome even for small bandwidth fields. Therefore, the UMPE model frequency shifts the center frequency to

15

d.c. The calculation becomes

$$\tilde{P}'_R(z,t) = \int P_{\omega,R}(z)\, e^{-i(\omega-\omega_o)t}\, d\omega \,, \tag{30}$$

where $\omega_o = 2\pi f_o$.

In practice, the model computes the FFT of $(1/\sqrt{R})\, \psi_{\omega,R}(z)$. Because this neglects the overall phase factor $e^{ik_o R} = e^{i\omega(R/c_o)}$, the time domain is heterodyned around the value $t_o = R/c_o$. Arrival times are then given as values of "reduced time", or $(t - t_o)$.

To minimize the effects of sidelobes due to a flat frequency spectrum, and of aliasing or wrap-around due to the finite BW, the UMPE model creates a Hamming window which is applied to the entire bandwidth. This method of tapering greatly reduces the effect of side lobes. Wrap-around effects may still be evident if the time window is not wide enough. The total length of the time window is

$$T = \frac{N}{BW} \tag{31}$$

where BW is the bandwidth of the source and N is the number of frequencies for which the model computes solutions, or the frequency FFT size if the FFT is padded with zeros. The frequency resolution is

$$\Delta\omega = \frac{BW}{N} = \frac{1}{T} \tag{32}$$

so the wider the time window needed, the finer the bandwidth must be resolved and the more total runs at different frequencies must be performed.

16

4.   Computing Exact, Two-Way Travel Times

The time domain arrival structure of the acoustic field at a given point in range and depth can be constructed from the Fourier synthesis of the full-spectrum complex field values calculated by UMPE at that range and depth over the frequency bandwidth.

In this manner, for every point on the bottom, a time series can be constructed which would show the arrival structure of the acoustic field from some source at a distance r = R from the point on the bottom.

Imagine a second source co-located at range R from the point on the bottom. If we label the bottom point b, and the two co-located sources r and s, then the arrangement would be as shown in Fig. 2.
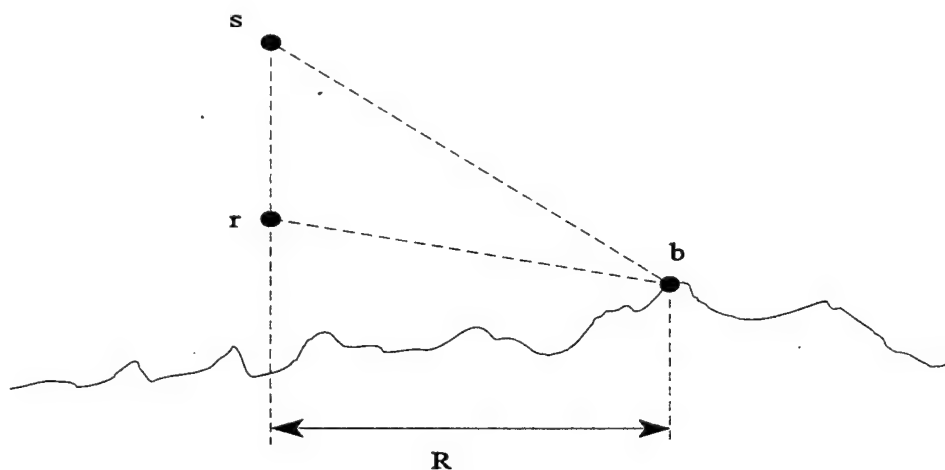
Figure 2. Source and Receiver Arrangement

The time series at a bottom point b from a source at location s could be constructed as previously shown. Also, the time series at receiver location r from a source at location b could be constructed in the same manner. By invoking reciprocity, the complex field at location r from a point source at b over a given frequency spectrum is the same as the complex field at location b from the same point source at r.

The time domain arrival structure of the complex acoustic field at location r from a source at point s would be a convolution of the time-domain arrival structures from s to b and from b to r:

$$\psi_2(t,R) = \int \psi_{sb}(t-\tau,R)\, \psi_{br}(\tau,R)\, d\tau \tag{33}$$

or, in the frequency domain:

$$\begin{aligned} \psi_2(\omega,R) &= \psi_{sb}(\omega,R) \times \psi_{br}(\omega,R) \\ &= \psi_{sb}(\omega,R) \times \psi_{rb}(\omega,R) \end{aligned} \tag{34}$$

where the subscript "2" stands for two-way, and $\psi_{br}(\omega,R) = \psi_{rb}(\omega,R)$ by reciprocity. $\psi_{rb}(\omega,R)$ and $\psi_{sb}(\omega,R)$ are the complex acoustic fields output by the UMPE model for all frequencies in the spectrum.

This development has assumed reflection of the field at only one bottom point. In reality, the arrival structure at point r is the summation of the convolved arrival structures for all range steps:

$$\psi_2(t) = \psi_2(t,r) + \psi_2\left(t+\frac{2\Delta r}{c_o},r+\Delta r\right) + \psi_2\left(t+\frac{4\Delta r}{c_o},r+2\Delta r\right) + \dots \tag{35}$$

18

where all time series developed for each step in range must be summed. For any given range R, the center time from the Fourier synthesis will be $T_c = R/c_0$ with a time window width of $\Delta T = 1/\delta f$ where δf is the incremental frequency spacing between each CW calculation. A range step was used to produce changes in T_c equal to an integer number of $\delta t = 1/BW$, the corresponding incremental sampling of the time window, i.e.

$$\Delta R = N c_o \, \delta t. \tag{36}$$

Therefore every time window computed for each range step will have time increments which overlap those at neighboring range steps.

The complete time series will be developed as defined in Eq. (35) where

$$\psi_2(t + \frac{2\Delta r}{c_o}, r + \Delta r) = \int \psi(\omega, r + \Delta r) \, e^{i\omega(t + \frac{2\Delta r}{c_o})} \, d\omega$$

$$\tag{37}$$

$$= FFT\left[\psi_2(\omega, r + \Delta r) \, e^{i\omega \frac{2\Delta r}{c_o}}\right].$$

In order to develop the full time series, the exponential factor immediately above will be left out of the actual calculation, and each subsequent range step contribution will simply be shifted in time so that its center time is $t = 2\Delta r/c$.

19

III. DATA ANALYSIS AND MODEL PREDICTIONS

A.   THE MODELED STUDIES CONDUCTED

In order to perform model predictions which can be compared to actual data, five segments were chosen from the ARSRP study [Ref. 3] which correspond to five distinct arrangements of towed source transmitting to a near-bottom vertical array. For all cases, the model source was placed at 181 meters depth, a source level of 232 dB re μPa/m was used, and bathymetry was extracted along the bearing from source to receiver in order to accurately simulate the true environment. The sound speed profile in the water column used by the model was taken from one of the CTD casts in the region, and the bottom was assumed to be homogenous with a sound speed, density, and attenuation of 1800 m/s, 2.0 g/cm^3, and 0.2 dB/m/kHz respectively.

For Segments 016, 031, and 046, the near-bottom vertical line array (VLA) was stationary as the Cory's source moved around it. The UTM coordinates (zone 23, based on the WGS-84 ellipsoid) for the near-bottom array were (377.43, 2888.51). The source for Segment 016 was located at UTM coordinates (383.82, 2901.80) so that the range from source to receiver was 14.75 km. The source for Segment 031 was located at (398.03, 2899.89) and the separation range was 23.53 km. The source for Segment 046 was located at (388.66, 2885.01) and the separation range was 11.76 km.

For Segments 544 and 564, the near-bottom VLA was located at UTM coordinates (192.27, 2944.86). The source for Segment 544 was located at (223.2, 2953.54) and the

21

separation range was 32.12 km. The source for Segment 564 was located at (210.36, 2932.48) and the separation range was 21.92 km.

Plots of the transmission loss fields of the ocean cross-sections along the radials of the five segments were made at the center frequency of 227.5 Hz. These fields are calculated by the UMPE model and show the propagation of the acoustic energy from the source outward.

Segment 016's arrangement, shown in Fig. 3, places the near-bottom array at 14.75 km, which is prior to one-half convergence zone (CZ) distance. The bottom profile for this radial is relatively smooth with a slight upslope along the latter half of the calculation distance.

Segment 031's arrangement, shown in Fig. 4, places the near-bottom array at 23.53 km, just prior to one-half CZ distance. The propagation in this case is bottom-limited at 25 km. The bottom profile for this radial shows an almost flat bottom along the mid-point with gradual rises of approximately 1500 meters near source and receiver locations. The forward scatter resulting from interaction with the bottom can be dimly seen in the top right of the figure of which some reflects off the surface back down to the location of the array near the bottom.

Segment 046's arrangement, shown in Fig. 5, places the near-bottom array at 11.76 km which is well before the one-half CZ range. The bottom profile shows several larger-scale bottom features in the first half of the radial distance.

Segment 564's arrangement, shown in Fig. 6, places the receiver array at 21.92 km, prior to one-half CZ distance. The bottom profile shows a gradual downslope from
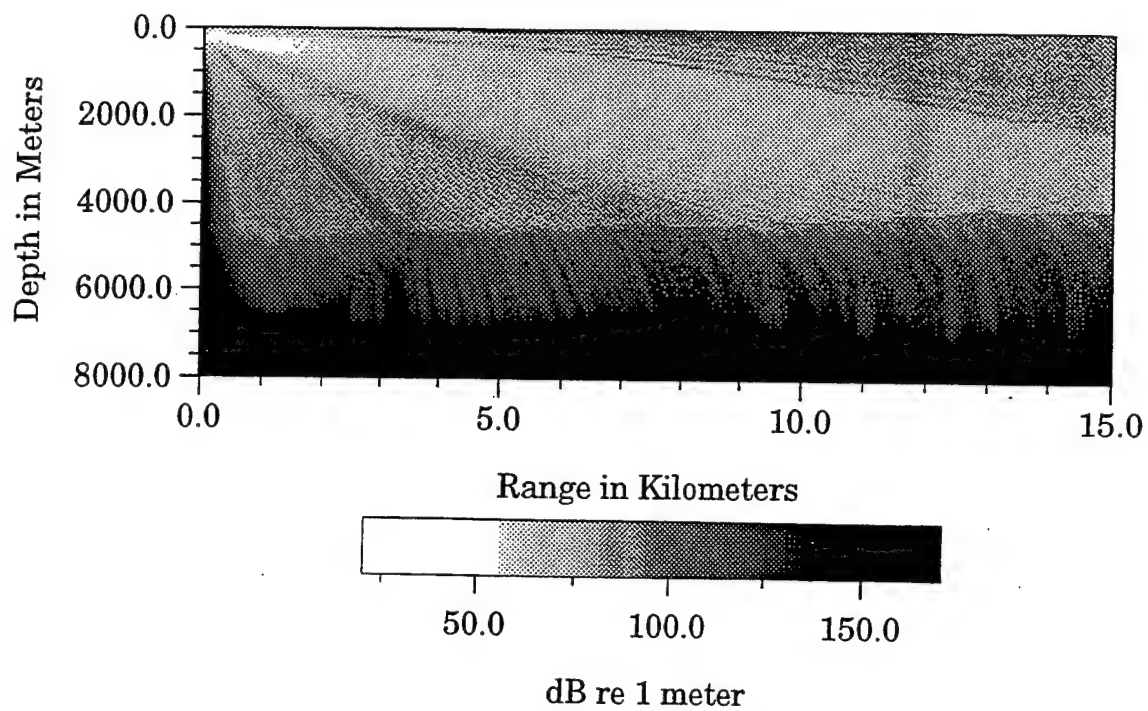
22

Figure 3. Segment 016 Transmission Loss Field for the Array Source.
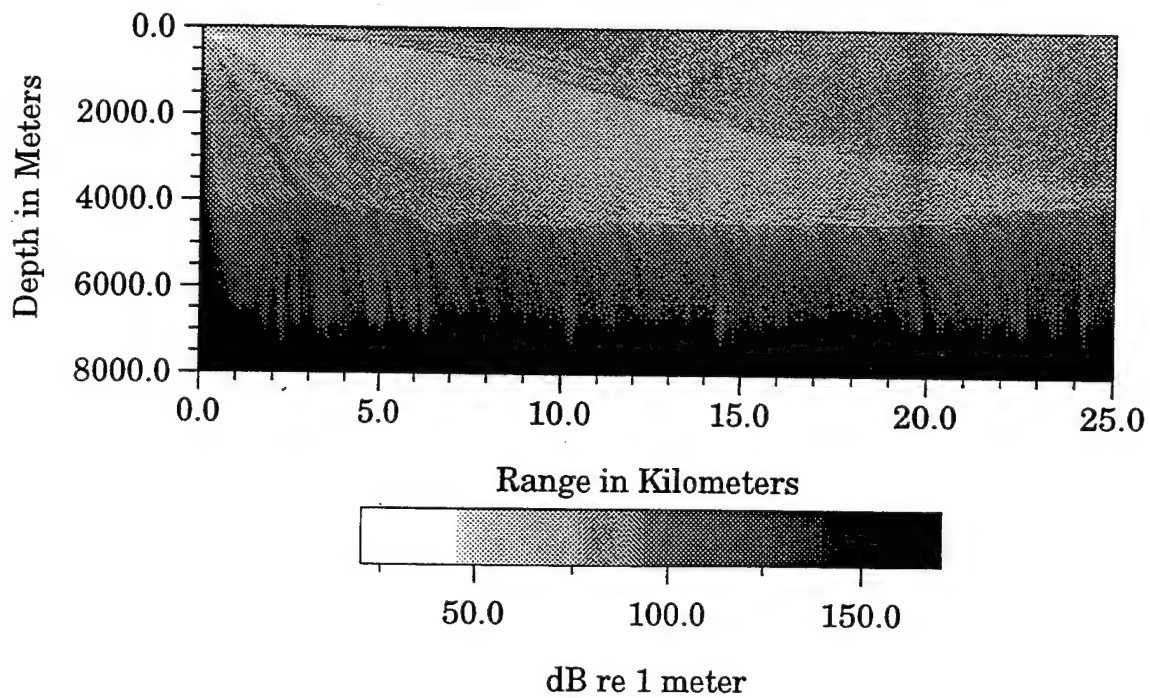

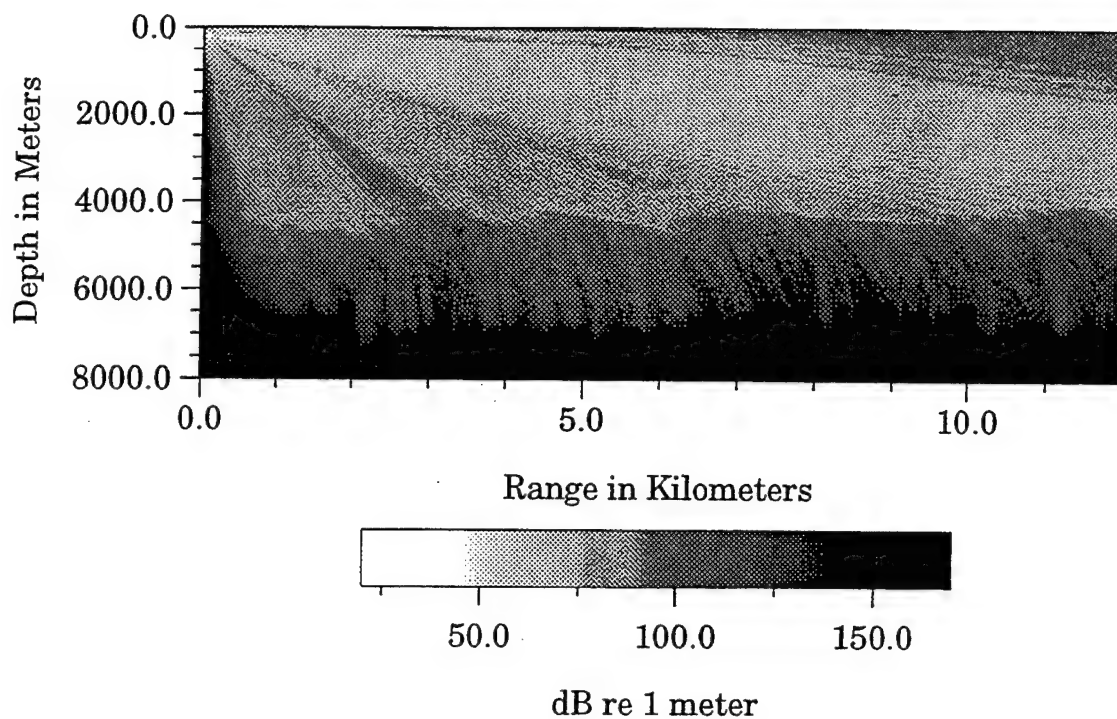Figure 4. Segment 031 Transmission Loss Field for the Array Source.

23

Figure 5. Segment 046 Transmission Loss Field for the Array Source.
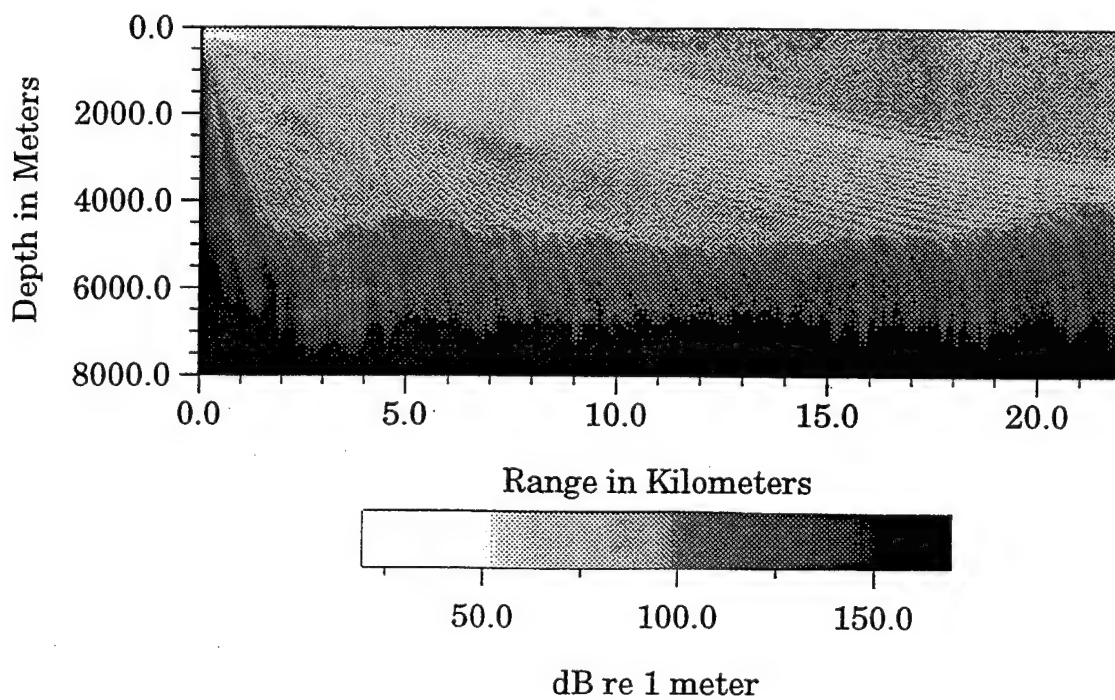

Figure 6. Segment 564 Transmission Loss Field for the Array Source.

5-10 km and a gradual upslope over the last quarter of the radial distance, with no large-scale features interrupting the relatively smooth profile.

Segment 544's arrangement, shown in Fig. 7, has one of the most interesting bottom profiles with several major large-scale features from which reflected energy paths can be clearly seen. The receiver array is located at 32.12 km, just past one-half CZ distance. In this case propagation is bottom-limited at ~30.5 km, prior to the array location. Figure 8 shows the UMPE model prediction of the approximately 200-255 Hz broadband pulse arrival transmission loss structure over the entire water column at the range of the near-bottom VLA. The separation between primary and secondary bottom interactions is observed to be roughly 1.5 seconds.

B. EXISTENCE OF SECONDARY MULTIPLE ARRIVALS

Initially, the transmitted pulse in all cases can be considered a single wavefront in time. The highest energy level is transmitted horizontally from the source and occupies the higher, more shallow end of the pulse. As the pulse propagates the bottom end undergoes a bottom reflection which begins to spread the signal's range resolution. Further downrange, this forward scattered energy reflects from the surface and again interacts with the bottom. This propagation is explained in detail in Ref. [4].

The range resolution of this secondary interaction has been much degraded as the pulse has become spread out over some range. Also, this secondary interaction is occurring at the same time the primary direct-path pulse is ensonifying a patch of seafloor
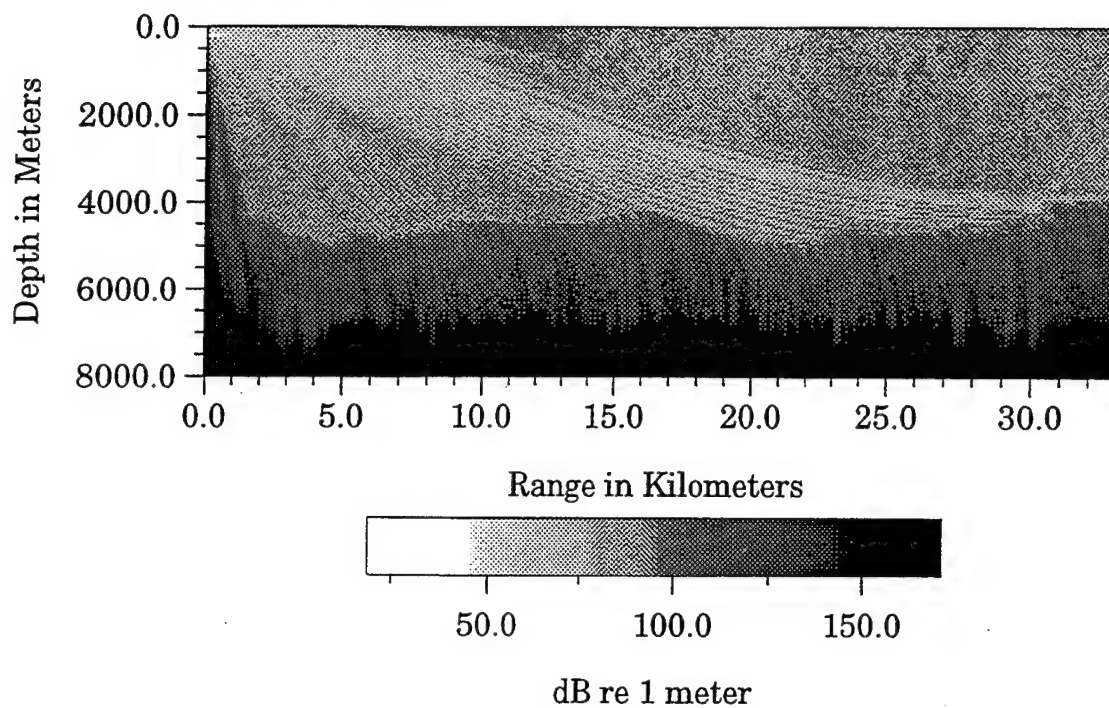
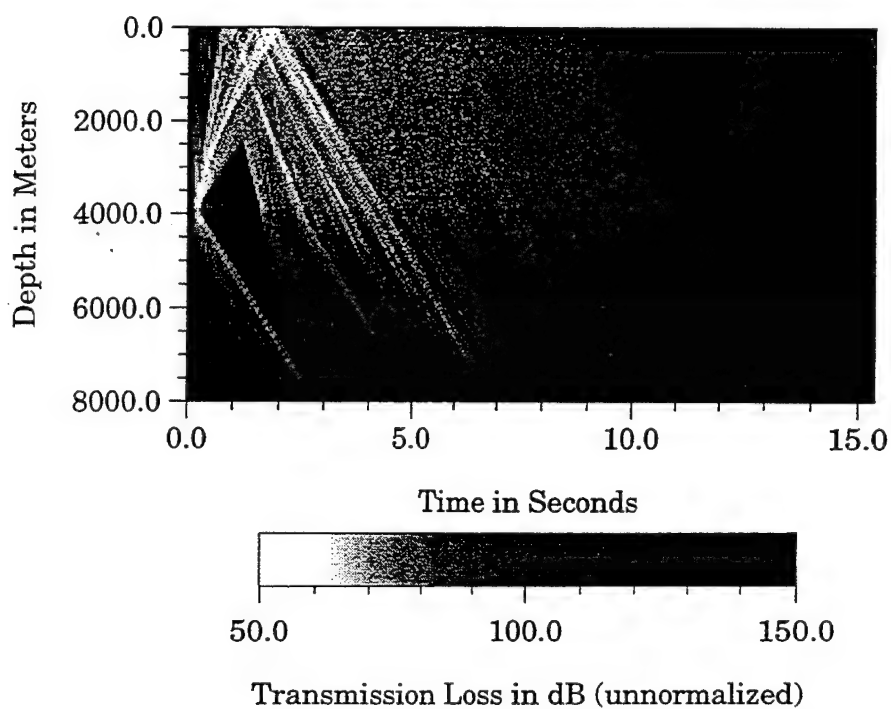Figure 7. Segment 544 Transmission Loss Field for the Array Source.

Figure 8. Segment 544 Broadband Arrival Structure at 32.12 km.

26

further downrange. Since the reciprocal paths of both the primary and secondary interactions back to a monostatic receiver platform will arrive at the same time, discrete scattering events at the position of a primary interaction will be contaminated or combined with scattering events at different places on the seafloor. These secondary interactions occur at higher angles of incidence and, because of this, may have their scattering strengths enhanced.

The effects of these secondary interactions are most significant at ranges of one-half CZ and greater. In cases where the propagation is not bottom-limited, or where the primary portion of the pulse is forward scattered, the highest level of ensonification beyond the range of primary interactions will be due to the secondary interactions instead of the primary. The returns from these interactions can result in reverberation features being mapped beyond the true point of contact by several kilometers.

By looking at the data recorded by the near-bottom VLA's in the vicinity of one-half CZ, such phenomena can be verified. The ability to beamform the data allows the primary, near-grazing interaction to be distinguished from the secondary, higher-angle arrivals undergoing multiple reflections.

Data from the five simulated segment runs has been extracted over the aperture of the actual near-bottom VLA (120 meters long, approximately 100 meters off of the bottom). Vertical spacing of the model data required 63 depth elements to be extracted to simulate the complete aperture of the near-bottom VLA. This data was then beamformed as explained in Chapter II to yield plots of transmission loss arrival structures for the five segments.

Figure 9 shows the beamformed predicted arrival structure for Segment 016. Values of transmission loss in dB (unnormalized) outside the plotted scale are assigned the maximum or minimum values for the plot as appropriate. The exact normalization factors for transmission loss (TL) values are unknown due to the process of beamforming the data, but all modeled and beamformed values are accurate relative to each other. Positive angles indicate propagation from the bottom towards the surface, i.e. energy coming up from below these element depths. The initial direct path arrival is so intense that the sidelobe structure has spread over multiple adjacent angles and times. The next set of arrivals occurs roughly 2.5 seconds later and exhibits a symmetry about grazing with lower intensity and more diffuse arrivals from below (positive angles). The arrivals from below are more diffuse due to an extra reflection from the bottom just prior to reaching the array. These secondary arrivals tend toward higher arrival angles with increasing time as expected due to the increased path lengths they must travel. In addition to these features, there is also some structure which tends toward more grazing angles with time. This seems to originate from a point of high-intensity incidence which also produces the expected increasing angle with time features. The cause of this unexpected feature is not well understood, though all features must be the result of forward scatter since the model does not compute any back-scattered effects.

The match-filtered and time-domain beamformed LFM signal arrival structure received by the VLA for Segment 016 is shown in Fig. 10. The primary arrival occurs at 0.4 seconds and shows earliest arrivals from above (negative angles) with later arrivals occurring as the arrival angle passes through zero to positive values, which also matches
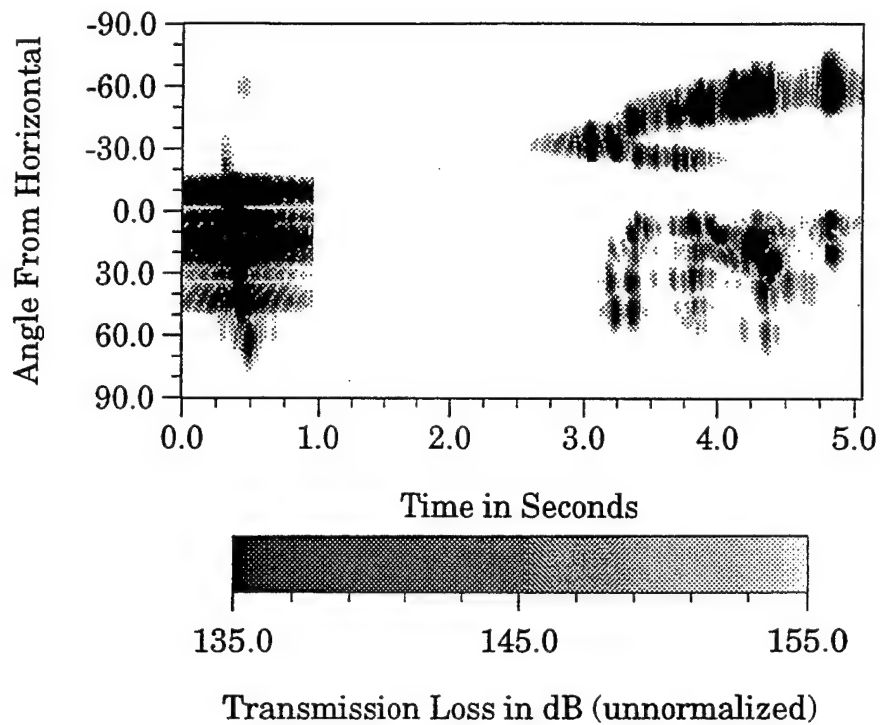
28

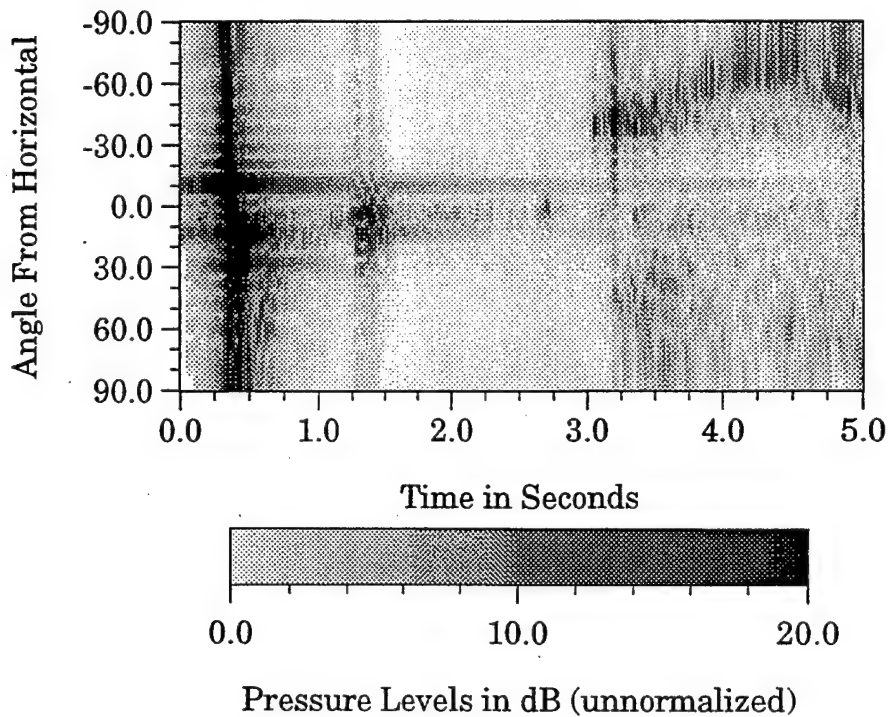Figure 9. Segment 016 Beamformed Arrival Structure.

Figure 10. Segment 016 Beamformed VLA Arrival Structure.

29

with model predictions. The structure seen at 10° and 1.3 seconds is most likely backscatter from some bottom feature just past the VLA. This structure does not show up in Fig. 9 as the model only calculates forward scatter. Secondary arrivals occur approximately 2.8 seconds after the primary and exhibit the same structure as described above for the model predictions of Fig. 9.

Figure 11 shows the beamformed predicted arrival structure for Segment 031. The general pattern is the same, though the second set of arrivals, which occurs roughly 1.5 seconds after the primary arrival, is more spread out in time as would be expected for the longer propagation range.

The match-filtered and time-domain beamformed LFM signal arrival structure received by the VLA for Segment 031 is shown in Fig. 12. The primary arrival occurs at 0.25 seconds, there exists some backscatter structure at 1.5 seconds, and secondary arrivals show up 1.8 seconds after the primary arrivals. This shows good overall agreement with the model predictions shown in Fig. 11.

Figure 13 shows the beamformed predicted arrival structure for Segment 046. Secondary arrivals first appear 2.8 seconds after the primary. The match-filtered and time-domain beamformed LFM signal arrival structure received by the VLA for Segment 046 is shown in Fig. 14. Again, arrival angles and time between primary and secondary arrivals agree very well.

Figures 15 and 16 show the beamformed predicted arrival structure for Segment 544. No actual beamformed data was available for this segment. The model predictions conducted have a frequency spacing which results in a total time window of 15.36
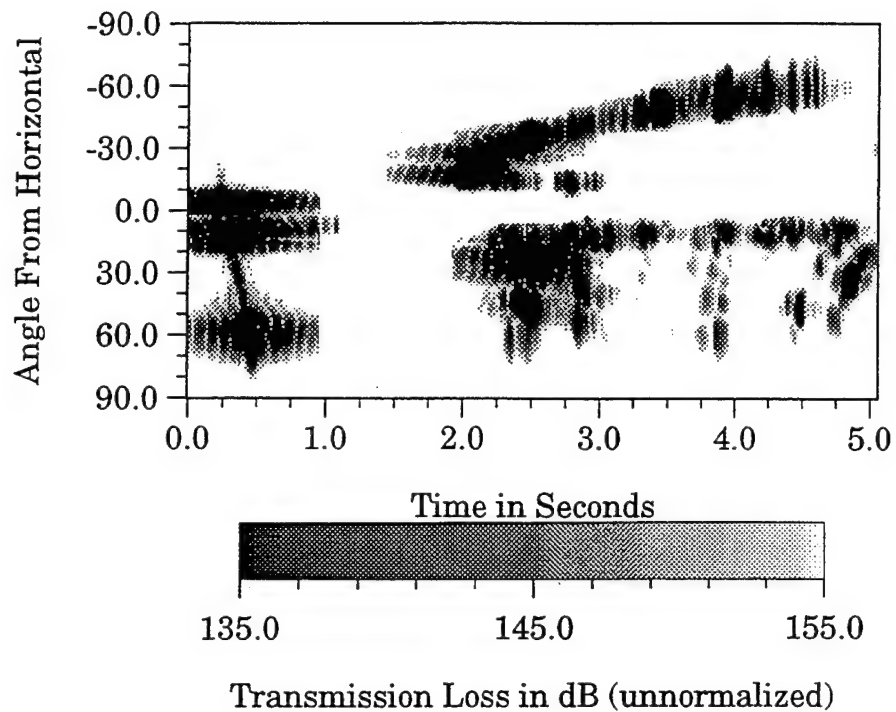
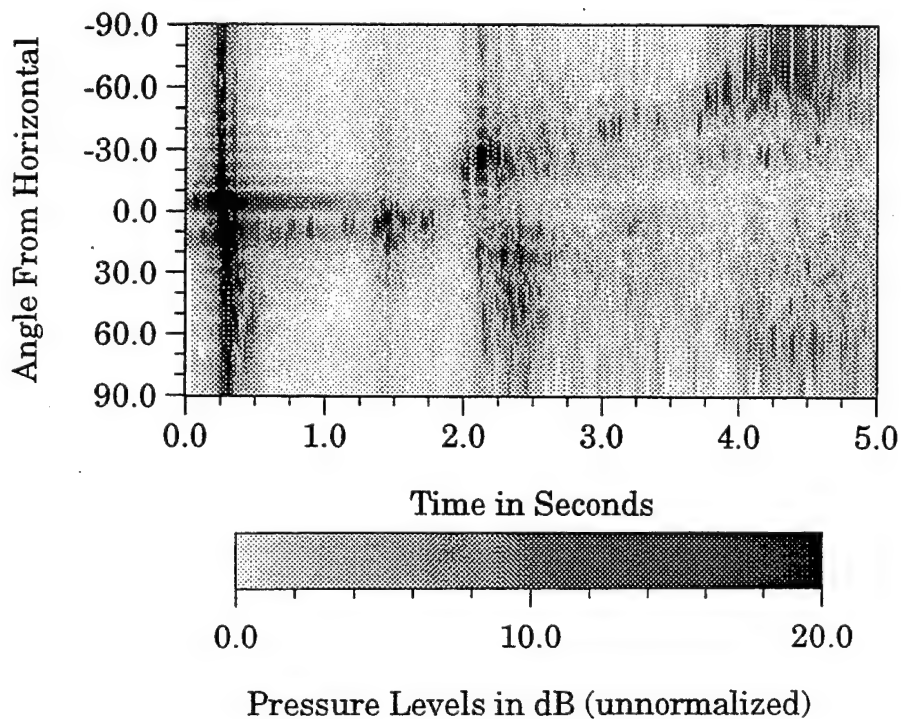Figure 11.   Segment 031 Beamformed Arrival Structure.

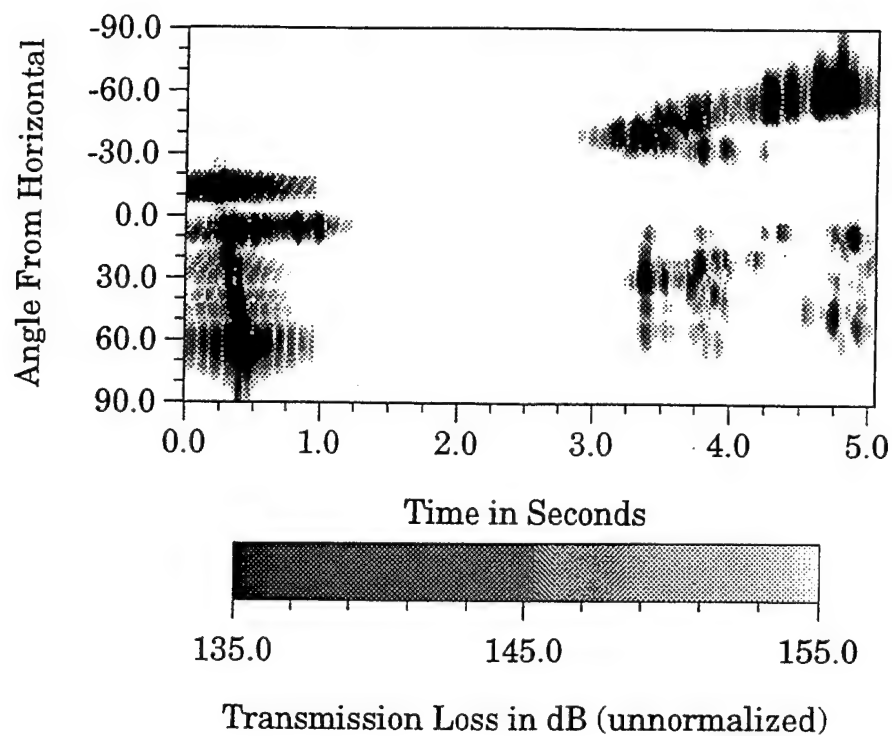Figure 12.   Segment 031 Beamformed VLA Arrival Structure.

31

Transmission Loss in dB (unnormalized)

Figure 13. Segment 046 Beamformed Arrival Structure.

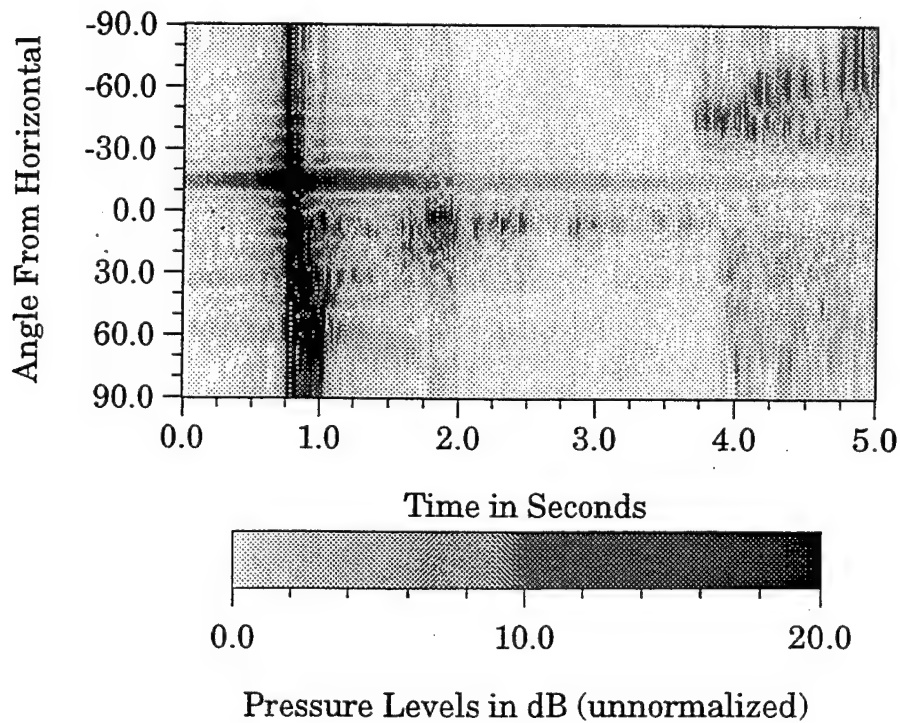Pressure Levels in dB (unnormalized)
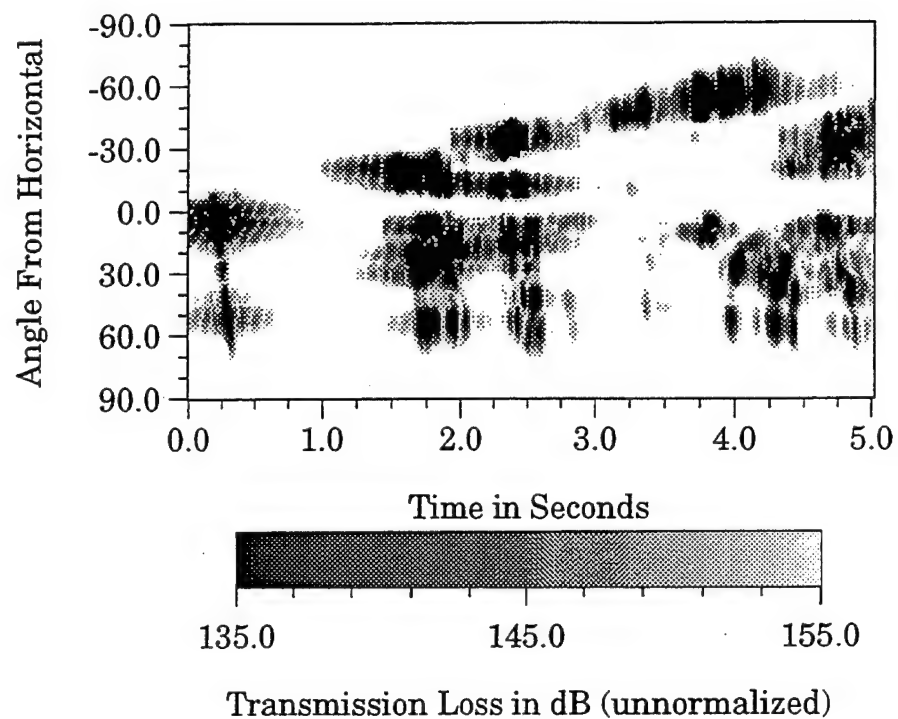
Figure 14. Segment 046 Beamformed VLA Arrival Structure.

32

Figure 15. Segment 544 Beamformed Arrival Structure.

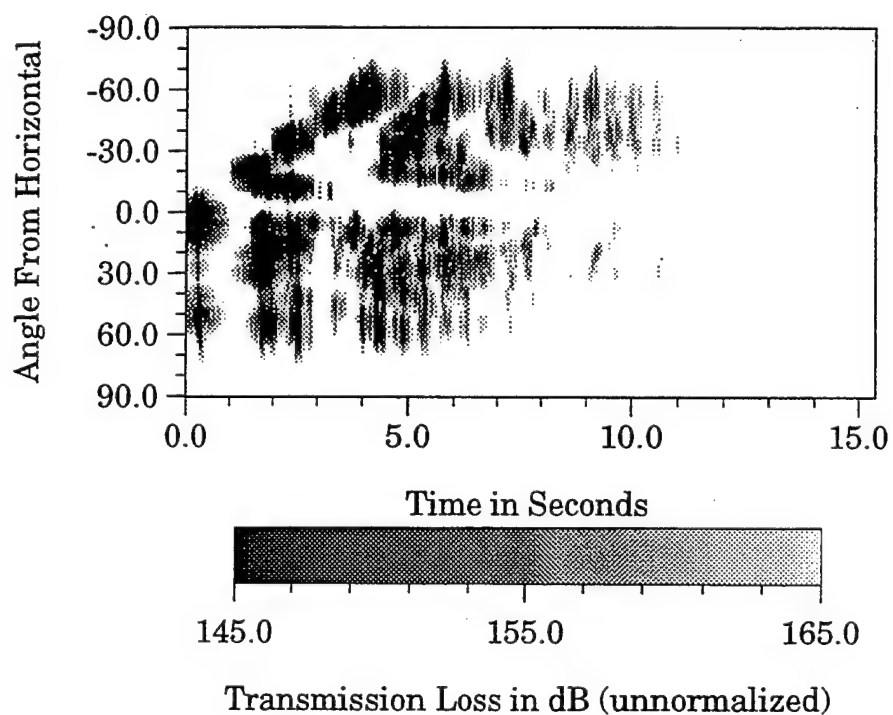Figure 16. Segment 544 Complete Beamformed Arrival Structure.

33

seconds, and this longer time window is shown in Fig. 16. There exists a third, fourth, and possibly a fifth distinct arrival structure, each of which arrives at progressively higher angles and with less time separating each subsequent set of arrivals. Comparison of the full time windows of beamformed modeled data shows that in general, the farther out in range from the source, the shorter the time interval between the primary and first secondary arrivals; the more spread out in time these secondary arrivals; and the shorter the time between subsequent sets of secondary arrivals, all of which must result from forward scatter. For the purpose of this thesis, only the secondary multi-path arrivals which occur at or close to the same time as the primary arrival are of concern.

Figure 17 shows the beamformed predicted arrival structure for Segment 564 and Fig. 18 shows the match-filtered and beamformed data from the near-bottom VLA for this segment. Given that the predicted arrival structures for all five segments are the result of only forward propagation calculations, there is significant agreement between predicted and actual arrival structures for all cases, showing that these secondary arrivals do indeed exist and can affect two-way mapping resolution.

C.   INFLUENCE OF SECONDARY INTERACTIONS

The existence of secondary arrivals has been clearly shown in the previous section. To what extent do these secondary arrivals degrade the return signal at the receiver in a monostatic arrangement?
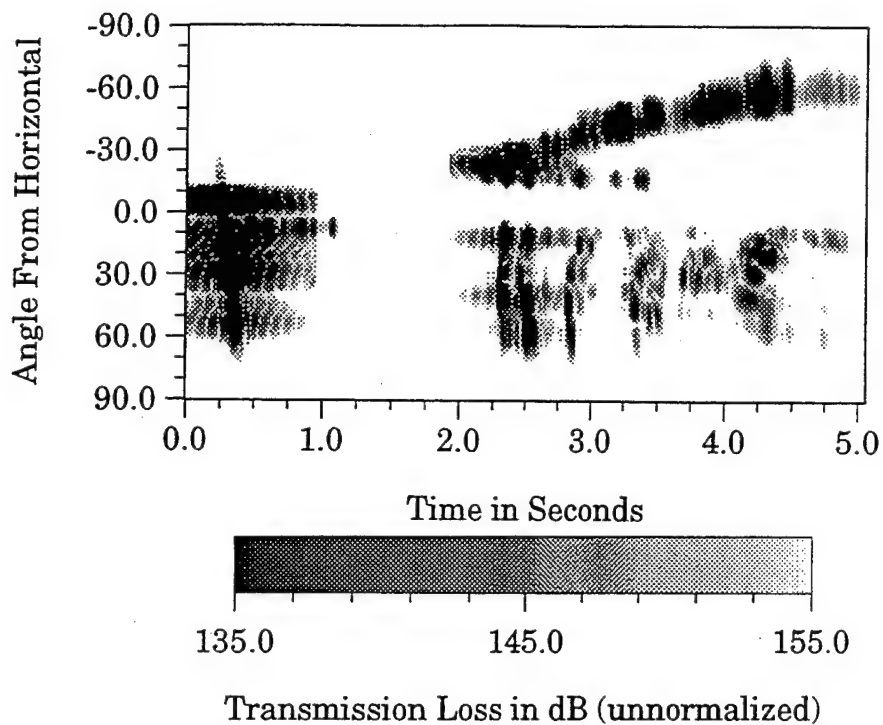
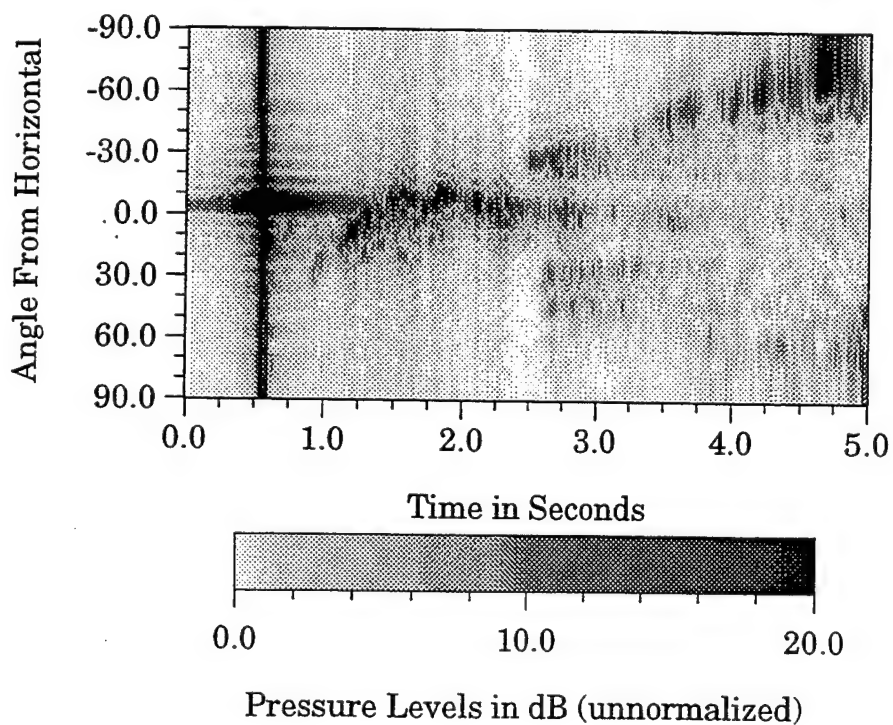Figure 17. Segment 564 Beamformed Arrival Structure.

Figure 18. Segment 564 Beamformed VLA Arrival Structure.

In an attempt to answer this, exact two-way travel time arrival signal levels were calculated for Segments 016 and 544 as explained in Chapter II. In order to ensure that a Fourier-transformed time window would be large enough to capture the complete structure of the two-way propagation out to the farthest range needed, frequency spacing for the UMPE modeling runs to determine exact two-way travel times was halved so that there were 2048 frequencies centered at 227.5 Hz with a total bandwidth of 66.66 Hz, resulting in a total Fourier-transformed time window of 30.72 seconds.

The exact two-way travel time structures and corresponding bottom profiles for Segments 016 and 544 are shown in Figs. 19-22. There is much more structure in both Figs. 19 and 21 than exists for the corresponding bottom profiles. This is an indication of the high degree of complexity in the ensonifying field. The fact that such complexity can exist distinct from any fine-scale bathymetric roughness is described in more detail in Ref. [4]. Large features can be discerned by large-scale arrival structures and trends in the return signal, but small-scale features corresponding to the "spiky-ness" of the return signal simply do not exist in the modeled bathymetry. Lobe structure from the source array as seen in Fig. 3 is the cause of the return signal's general appearance of very low return up to approximately 4 km, stronger returns from 4 to 10 km, and strongest returns from 10 to 15 km, the maximum range considered.

In an attempt to remove the majority of secondary interactions from the propagation, the UMPE code was modified for each segment to effectively remove the bottom interface up to a range of five kilometers in front of the near-bottom VLA's. This was done by matching water and bottom densities and sound speeds along the radial
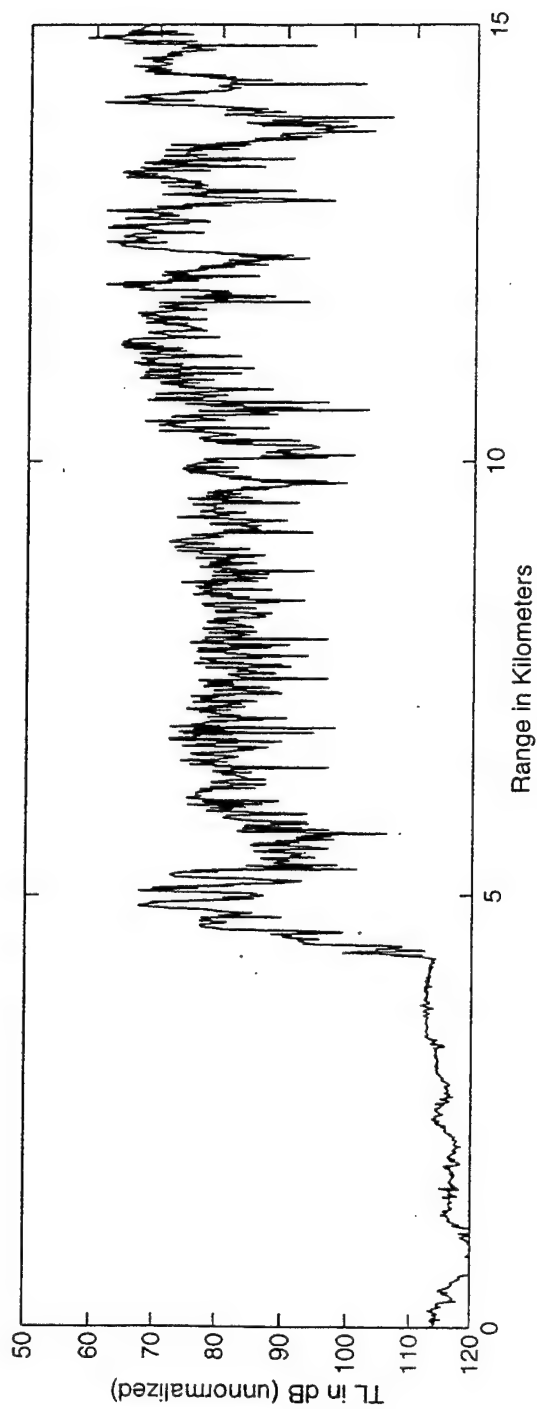
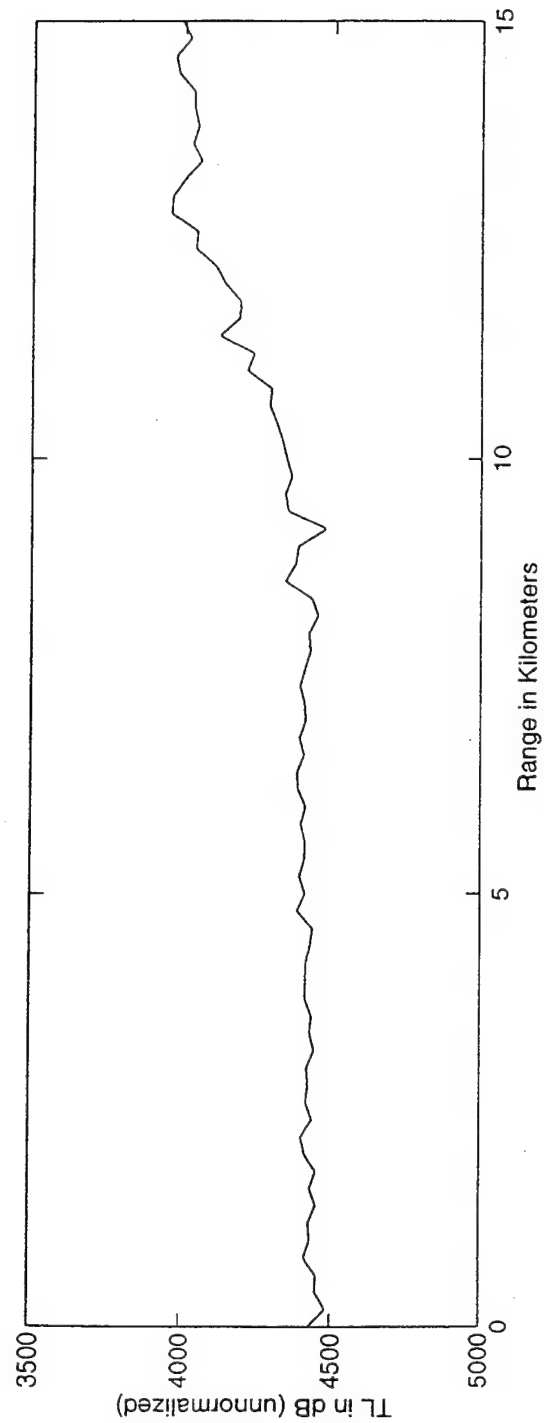Figure 19. Segment 016 Two-Way Exact Travel Time Structure.
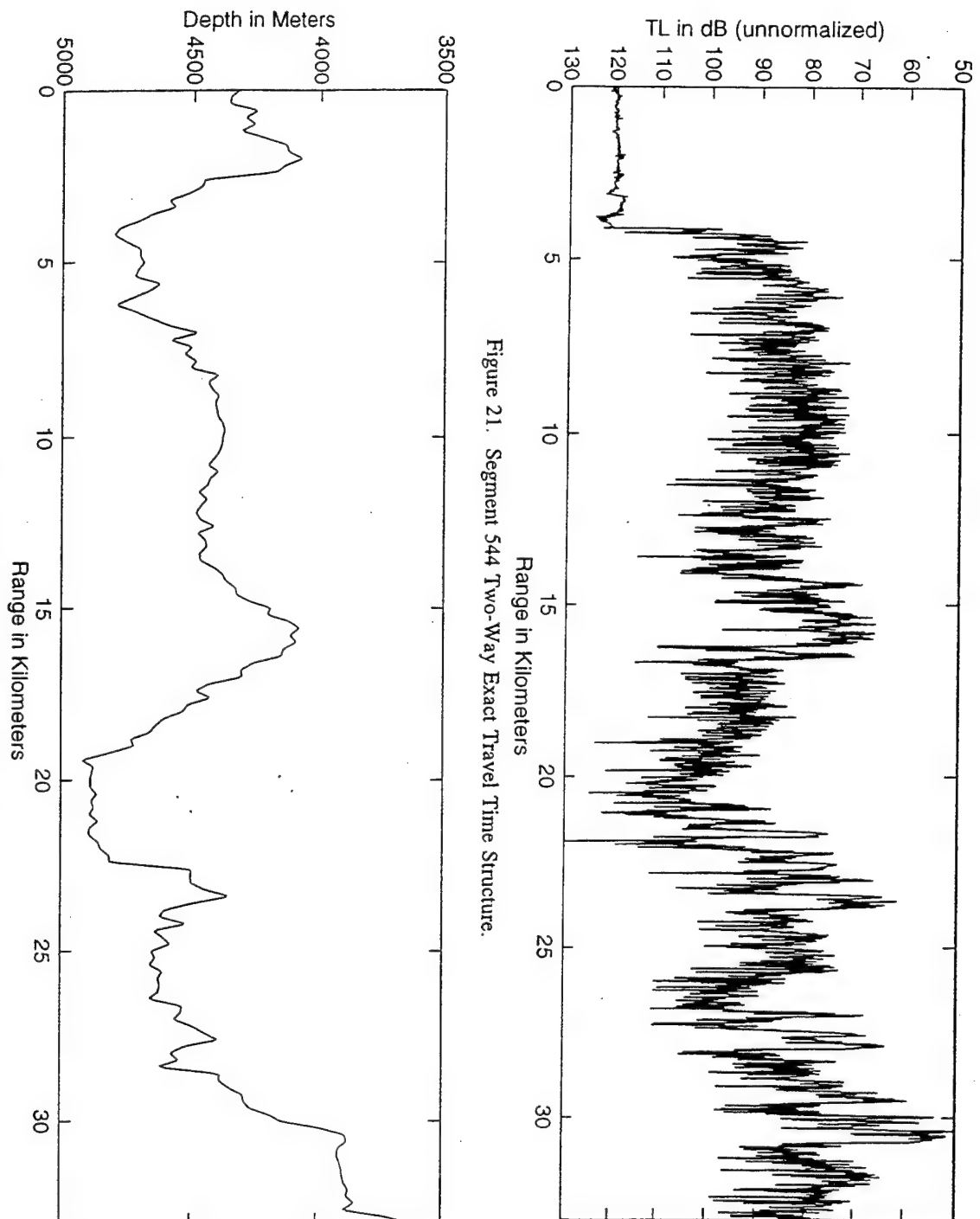

Figure 20. Segment 016 Bottom Profile.

37

Figure 21. Segment 544 Two-Way Exact Travel Time Structure.

Figure 22. Segment 544 Bottom Profile.

38

range. At five kilometers prior to the VLA, the bottom properties were linearly changed so that within three kilometers of the VLA, the bottom properties were the normal values used in the previous runs as stated earlier in the chapter. Though the bottom interface was removed, energy entering the ocean bottom was still attenuated as before. The results of altering the bottom properties for these segments on the propagation of acoustic energy can be seen in Figs. 23 and 24 which show the transmission loss fields of the ocean cross-sections along the radials of the two segments at the center frequency of 227.5 Hz.

Figure 23 shows the propagation along Segment 016. Surface reflections still occur, but any energy reflected from the surface near the source would hit the bottom interface prior to the VLA in the altered bottom region and be attenuated. With multipath energy removed, the propagation paths of the primary energy close to the surface can now be clearly seen. The three primary propagating lobes of the vertical array source are distinct, and the interference pattern resulting from Lloyd's mirror effect of the surface-reflected energy within the lobes is also more distinct. Figure 24 shows the propagation along Segment 544. Bottom-reflected energy just prior to the VLA can be seen to reflect from the surface and travel back down to ensonify the region beyond 31 km range. This region sees little of the primary energy which is bottom-limited around 31 km.

Figures 25 and 26 compare the unaltered bottom signal return and the altered bottom signal return for Segment 016. At ranges approaching 15 km, the same large structure exists in the returns, while in Fig. 25 it can be seen that multipath effects tend
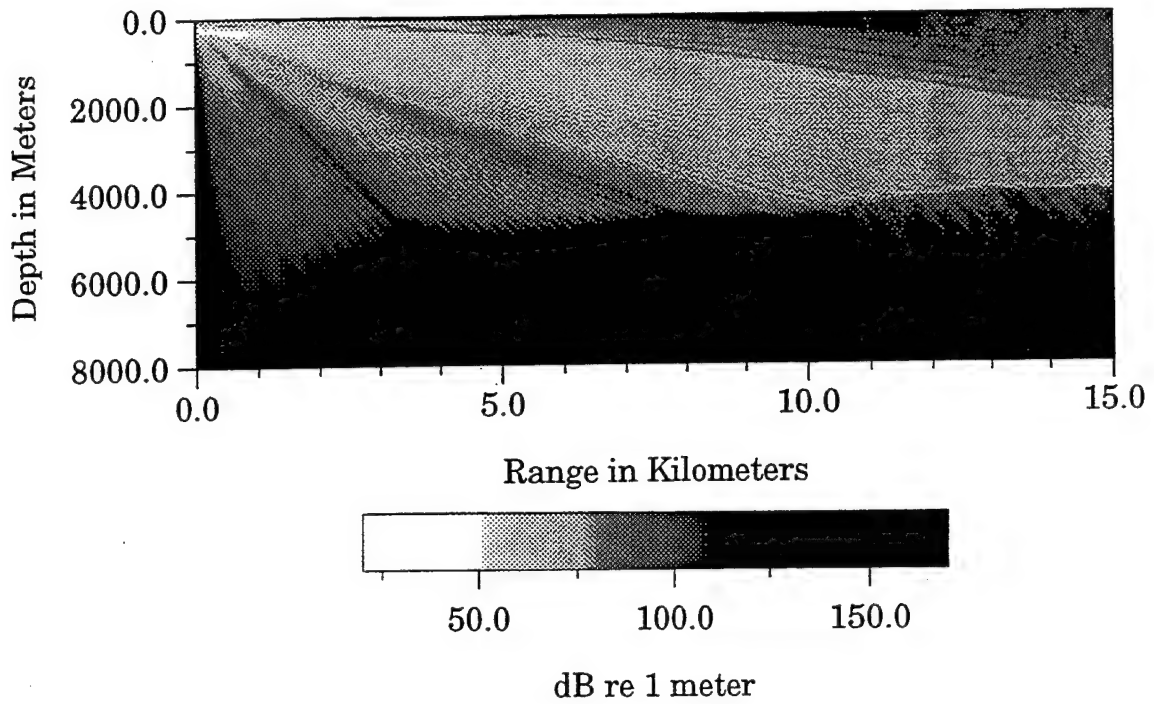
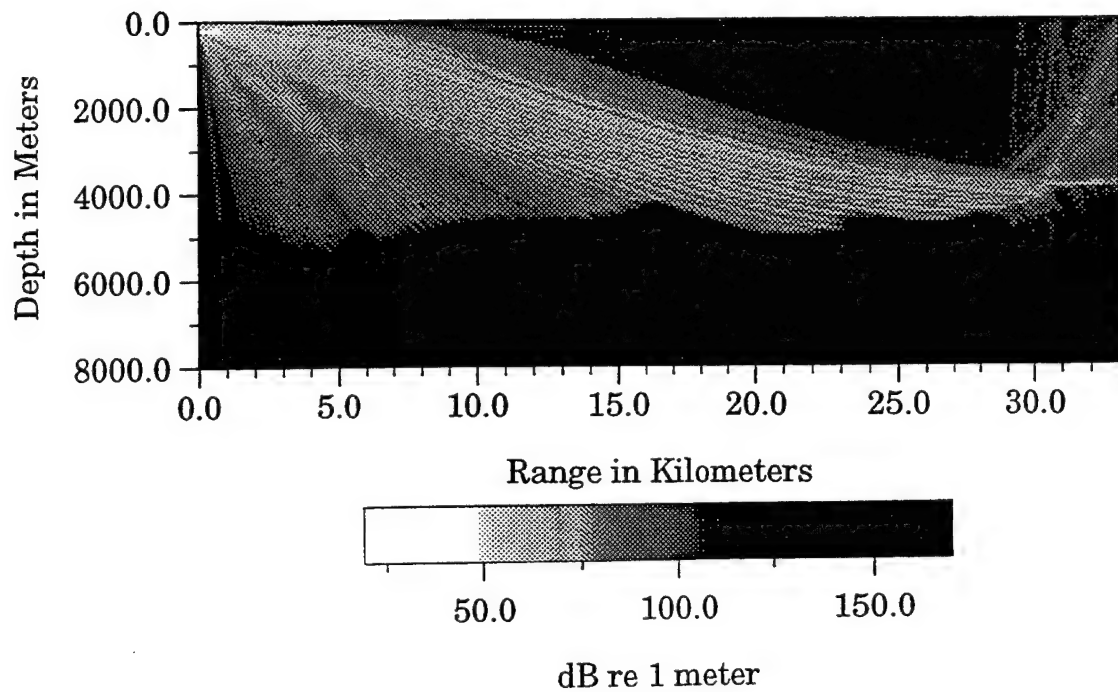Figure 23. Segment 016 Transmission Loss Profile - Altered Bottom.

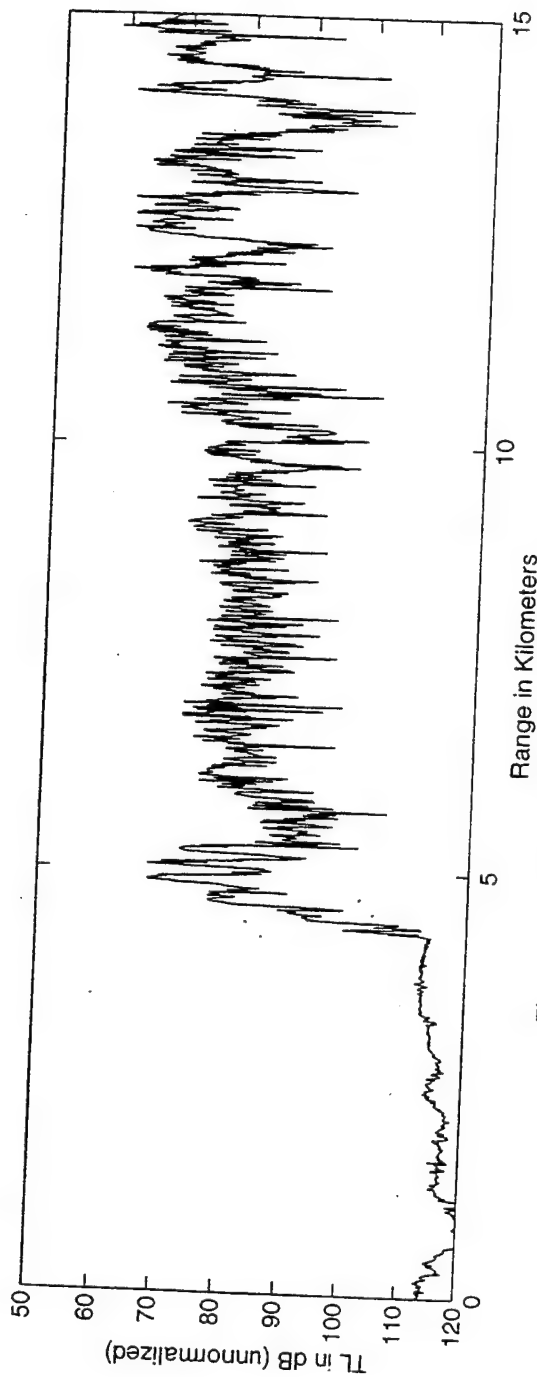Figure 24. Segment 544 Transmission Loss Profile - Altered Bottom.

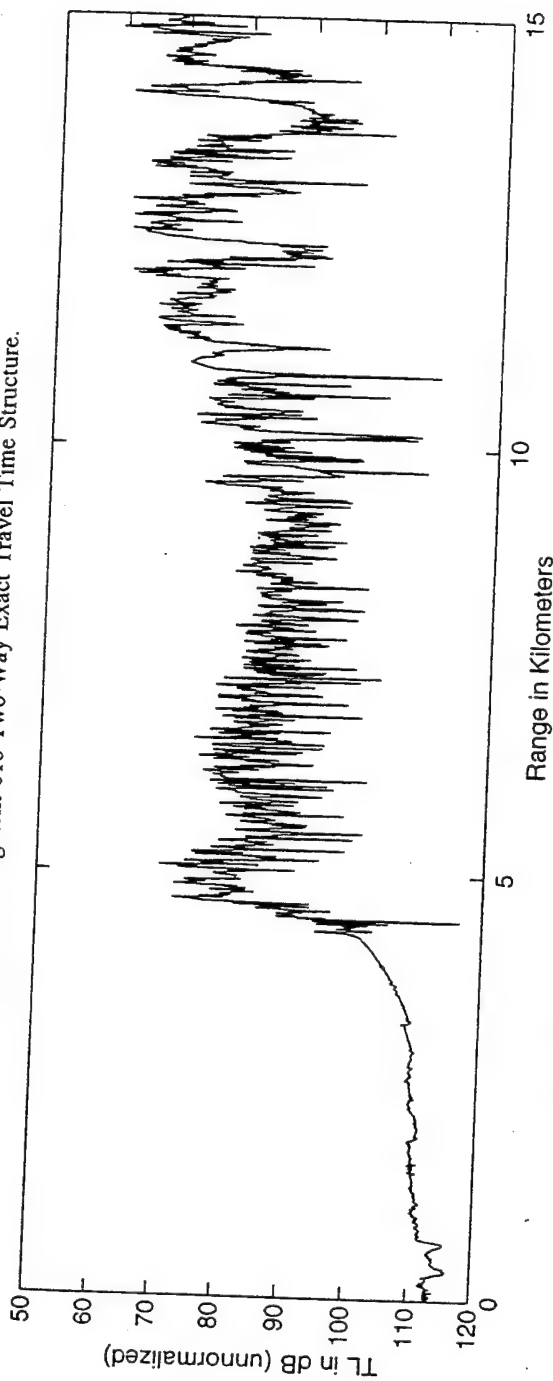Figure 25. Segment 016 Two-Way Exact Travel Time Structure.

Figure 26. Segment 016 Two-Way Exact Travel Time Structure - Altered Bottom.

41

to fill in the areas of low primary signal return, adding up to 5 dB of return in some cases. While the effect of the secondary, multipath arrivals is not very significant at these short ranges, it is important to note the considerable differences in details in the region of the altered bottom. The distinction can be considered the difference between computing the total (incident, reflected, transmitted, and forward scattered) field at the interface versus computing only the incident field. To correctly predict reverberation levels, the total field at the interface must be computed.

Figures 27 and 28 compare the unaltered bottom signal return and the altered bottom signal return for Segment 544. Again, the general effects of source array lobe structure can be seen when compared to Fig. 7. In the range of approximately 17 to 21 km, signal returns in the unaltered bottom case are as much as 25 dB higher than the returns caused by primary interactions alone. By referring back to the CW field in Fig. 7, it is noted that a ridge structure is near 16 km. This would produce a shadow region in the 17-20 km range if only direct path ensonification were considered. However, secondary multipaths are predicted to significantly increase the levels in this region. Another interesting feature is that the primary return in the unaltered bottom case at the range of approximately 21 to 23 km is actually lessened by the multipath effects. This is presumably due to the difference between computing the total field versus only the incident field. Once again, the lower primary return at the range of 25 km due to a shadow zone behind a ridge at approximately 23 km has had as much as 30 dB added to it in Fig. 27 from the returns of secondary, multipath interactions being received at the same time as the primary return.
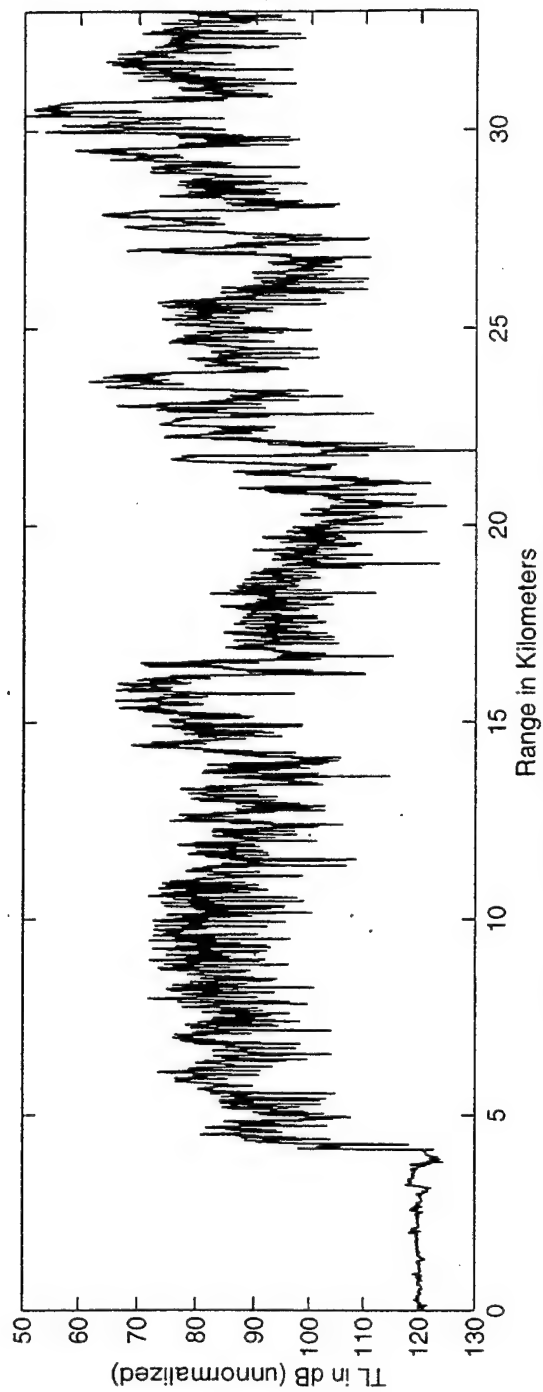
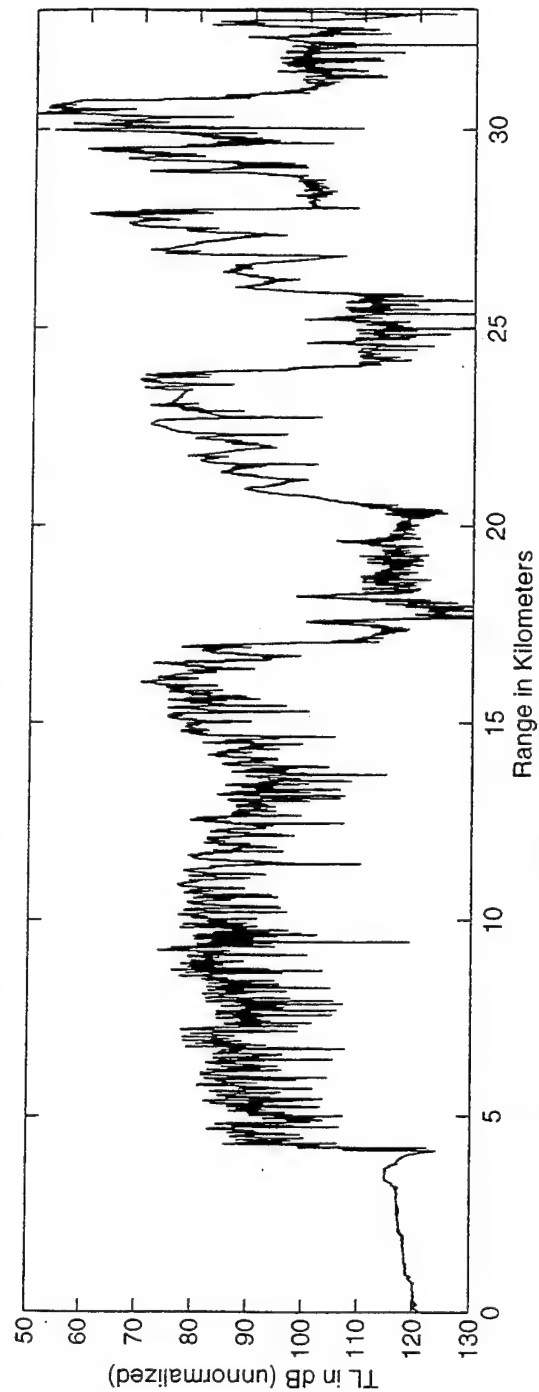Figure 27. Segment 544 Two-Way Exact Travel Time Structure.

Figure 28. Segment 544 Two-Way Exact Travel Time Structure - Altered Bottom.

43

Figures 29 and 30 show a magnified view of the unaltered bottom signal return and the altered bottom signal return, respectively, for Segment 544 for the ranges of 25 to 33 km. The secondary signal returns in Fig. 29 could result in some features being mapped to incorrect seafloor locations. The structure in Fig. 29 from 31 km to 32 km which exhibits the gradual upslope then downslope is actually from secondary returns occurring approximately 1.5 seconds later (see Figs. 8 and 15) from the large-scale ridge face at 30 km and would result in mapping another ridge structure at this location. This secondary "echo" was previously predicted in Ref. [4].
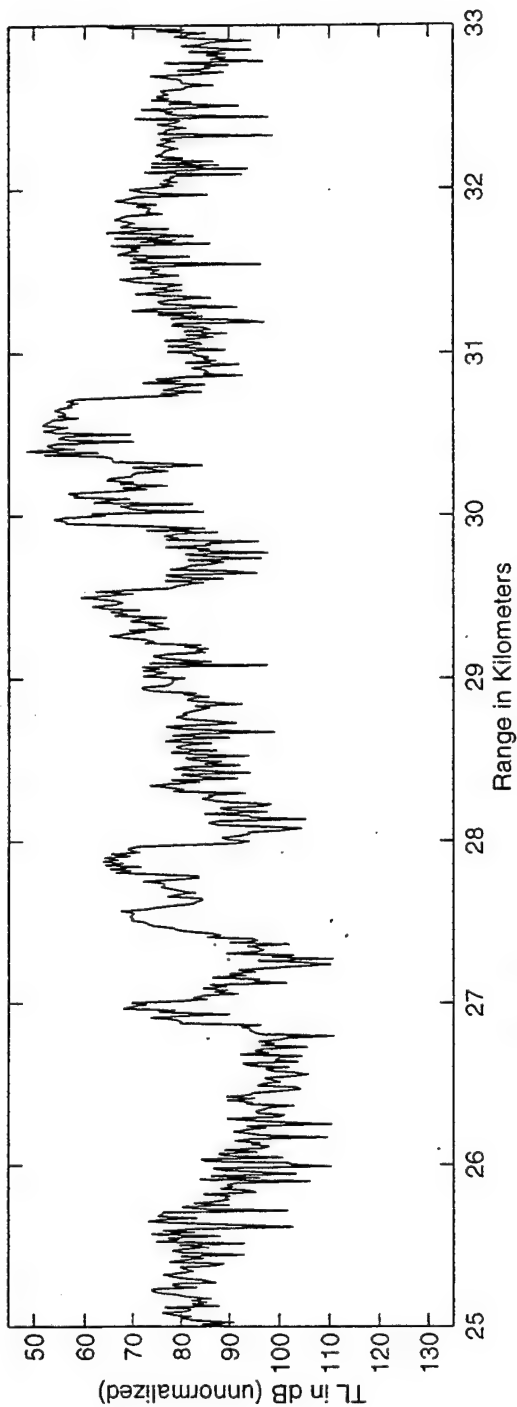
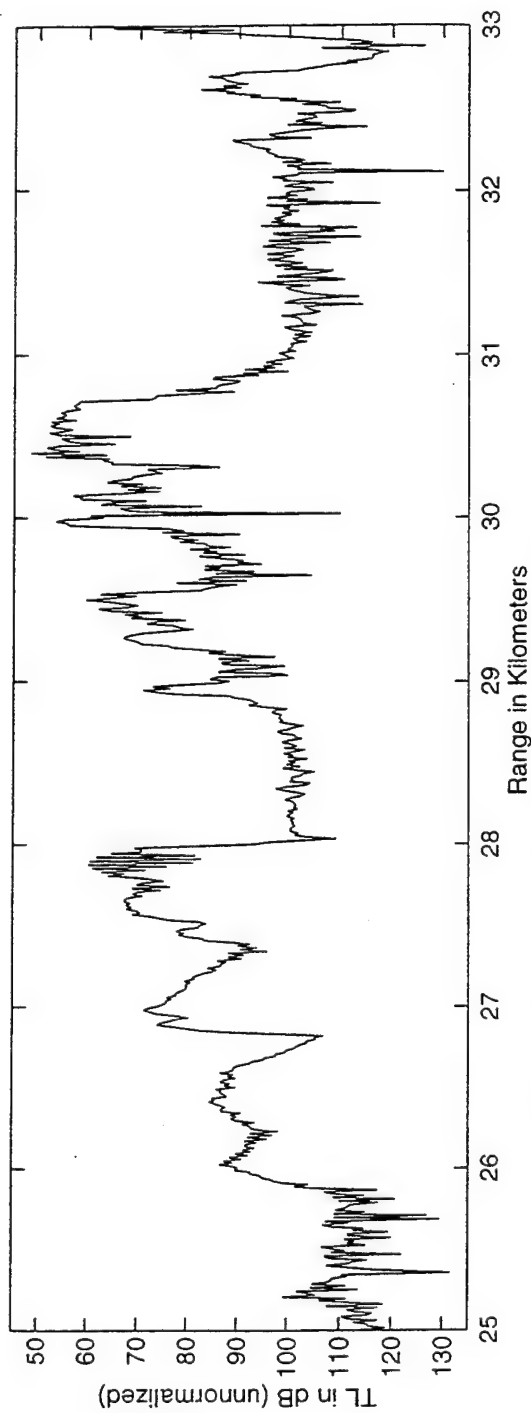Figure 29. Segment 544 Two-Way Exact Travel Time Structure.

Figure 30. Segment 544 Two-Way Exact Travel Time Structure - Altered Bottom.

45

IV. SUMMARY

It has been shown that the secondary arrivals predicted by the UMPE model do exist in the measured data. The exact two-way travel time calculations show that the levels of ensonification resulting from these secondary multipaths can be significant compared to the primary direct-path interaction at ranges near one-half CZ and greater. Furthermore, the exact two-way levels display a highly complex nature which are due to complicated ensonification structures rather than small-scale bathymetric features. The overall implication of this is that there are limitations on the ability to resolve discrete structures at ranges beyond a few water depths. These limitations arise from system limitations, processing techniques, and the inherently complex nature of the propagation.

One way to overcome some of these limitations in mapping resolution might be to use a vertical receive array, or some form of volumetric array, so that the ability to beamform in the vertical exists. Most secondary multipath interactions, at least those occurring during the return of the acoustic signal, will be arriving at higher angles than the direct-path returns so that they can be selectively rejected from the signal return.

Another aspect of the propagation which may affect the resolution of such a system is coupling between radials. This has not been considered in this research. Further studies incorporating azimuthal coupling should be conducted in an attempt to better understand the inherent problems associated with attempting to precisely map bottom bathymetry in this manner.

Finally, the shallow water environment is much different from the deep ocean environment and the modeling done for this thesis could be applied to shallow water cases to determine the effects of these secondary interactions. In a shallow environment, most of the propagation will be bottom-limited so multipaths will be the primary source of bottom ensonification. With the shift in emphasis toward the littoral environment for the Navy of the future, these issues will need to be addressed for improved sonar system performance on the submarines and ships of tomorrow's Navy.

LIST OF REFERENCES

1. Bottom/Subbottom Reverberation Science Plan (**1992**). ONR-ARSRP Symposium, La Jolla, CA, 7-9 April 1992.

2. *Office of Naval Research, ARSRP Initial Report, Acoustic Reconnaissance Cruise, 19 August 1991.*

3. *Office of Naval Research, ARSRP Initial Report, Acoustics Experiment, R/V Cory Chouest, 5-26 July 1993.*

4. Smith, K.B., Hodgkiss, W.S., and Tappert, F.D. (**1996**). "Propagation and analysis issues in the prediction of long-range reverberation," J. Acoust. Soc. Am., in press.

5. Ziomek, L.J. (**1995**). *Fundamentals of Acoustic Field Theory and Space-Time Signal Processing* (CRC Press, Boca Raton), Chap. 7.

6. Hardin, R.H. and Tappert, F.D. (**1973**). "Applications of the split-step Fourier method to the numerical solution of nonlinear and variable coefficient wave equations," SIAM Rev. **15**, 423.

7. Smith, K.B., Brown, M.G., and Tappert, F.D. (**1992**). "Ray Chaos in Underwater Acoustics," J. Acoust. Soc. Am. **91**, 1939-1949.

8. Smith, K.B. and Tappert, F.D. (**1993**). *UMPE: The University of Miami Parabolic Equation Model, Version 1.1*, MPL Technical Memorandum 432.

9. Bellman, R. (**1964**). *Perturbation Techniques in Mathematics, Physics, and Engineering* (Holt, Rinehart, and Winston, Inc., New York), pp. 38-39.

10. Thompson, D.J., and Chapman, N.R. (**1983**). "A wide-angle split-step algorithm for the parabolic equation," J. Acoust. Soc. Am. **74**, 1848-1854.

INITIAL DISTRIBUTION LIST

1.   Defense Technical Information Center. 2
Cameron Station
Alexandria, Virginia 22304-6145

2.   Library, Code 52. 2
Naval Postgraduate School
Monterey, California 93943-5101

3.   Kevin B. Smith, Code 33. 3
Naval Postgraduate School
Monterey, California 93943-5101

4.   Erick B. Cushman. 2
32 Country Club Blvd
Tuckerton, NJ 08087